Masters Theses   Graduate School

12-2012

Fatigue Behavior of High-Entropy Alloys

Michael Alexander Hemphill
mhemphil@utk.edu

Recommended Citation

To the Graduate Council:

I am submitting herewith a thesis written by Michael Alexander Hemphill entitled "Fatigue Behavior of High-Entropy Alloys." I have examined the final electronic copy of this thesis for form and content and recommend that it be accepted in partial fulfillment of the requirements for the degree of Master of Science, with a major in Materials Science and Engineering.

Peter K. Liaw, Major Professor

We have read this thesis and recommend its acceptance:

Hahn Choo, Yanwen Zhang

Accepted for the Council:
Carolyn R. Hodges

Vice Provost and Dean of the Graduate School

(Original signatures are on file with official student records.)

Fatigue Behavior of High-Entropy Alloys

A Thesis Presented for the
Master of Science
Degree
The University of Tennessee, Knoxville

Michael Alexander Hemphill
December 2012

ACKNOWLEDGEMENTS

Firstly, I would like to thank my parents, Bill and Jean Hemphill, for all of their love, patience, and support. You have been an inspiration to me and I thank you for everything you have done for Ben and me.

Secondly, I would like to thank my advisor, Prof. Peter K. Liaw for his guidance and support though these few years of my undergraduate and graduate studies. I appreciate everything you did for me and for pushing me to be a better student. I am grateful for Prof. Hahn Choo and Prof. Yanwen Zhang for serving on my committee. I would also like to thank all of Prof. Liaw's group members that have helped me with all aspects of my research, particularly Dr. Gongyao Wang for all of his help. I am appreciative to Prof. Jien-Wei Yeh and Dr. Che Wei Tsai from National Tsing Hua University, Taiwan, and to Prof. Tao Yuan from Ohio University, Athens, OH for all of their help with samples and analysis.

Much of the work presented here is based on the paper "Fatigue behavior of $Al_{0.5}CoCrCuFeNi$ high entropy alloys" written by the author [1].

ABSTRACT

Research was performed on the $Al_9Co_{18.2}Cr_{18.2}Cu_{18.2}Fe_{18.2}Ni_{18.2}$ [subscripts atomic percent] and $Al_{7.5}Cr_{22.5}Fe_{35}Mn_{20}Ni_{15}$ high-entropy alloys (HEAs) in an attempt to study their fatigue behavior. The present investigation shows encouraging fatigue-resistance characteristics due to their high fatigue lives of various samples at relatively high stresses. The current results indicate that the fatigue behavior of HEAs compares favorably to many conventional alloys, such as steels, titanium alloys, and advanced bulk metallic glasses with a fatigue-endurance limit of the $Al_9Co_{18.2}Cr_{18.2}Cu_{18.2}Fe_{18.2}Ni_{18.2}$ HEAs between 540 and 945 MPa and a fatigue-endurance limit to ultimate tensile strength ratio between 0.402 and 0.703. The $Al_{7.5}Cr_{22.5}Fe_{35}Mn_{20}Ni_{15}$ HEAs were found to have a fatigue-endurance limit between 540 and 630 MPa.

Some unpredictability in the fatigue life of the samples was observed by scattering in the stress versus life plot. Weibull models were applied to predict the fatigue data and to characterize the variability seen in $Al_9Co_{18.2}Cr_{18.2}Cu_{18.2}Fe_{18.2}Ni_{18.2}$ HEAs. A Weibull mixture predictive model was used to separate the data into two, strong and weak, groups. This model predicts that at stress ranges above 858 MPa, the median time to failure of specimens in the strong group will be greater than 10^7 cycles.

Large oxide particles were found on the tensile surfaces of both samples with microcracks forming at these sites. It was shown that these microstructural defects may have a significant effect on the fatigue behavior of HEAs. A

comparison of the endurance limits and fatigue ratios of HEAs to conventional structural alloys shows that HEAs may outperform many conventional alloys under fatigue conditions. It is believed that a reduction in the number of defects introduced during fabrication and processing may result in a superior fatigue behavior, which exceeds that of conventional alloys.

TABLE OF CONTENTS

LIST OF TABLES

LIST OF FIGURES

CHAPTER 1
Introduction

1.1   Definition of High-entropy Alloys

Most practical alloy systems are based on a single principal element to form the matrix of the system and the addition of various elements to enhance particular properties of the material, such as iron or copper-based alloys. This model greatly limits the number of viable systems and, thus, restricts the expanded use of alloying elements to obtain more desirable properties [2]. An alloy containing multiple principal elements was expected to yield many intermetallic compounds with the possibility of complex microstructures and with less desirable mechanical properties [3]. However, in high-entropy alloys (HEAs), these phases are not prevalent, and solid solutions based on multiple principal elements are possible [3-5].

Thermodynamically, a system reaches equilibrium when the Gibbs free energy of the system (ΔG_{mix}) reaches its global minimum. The mixing energy of a system is described by Equation 1,

$$\Delta G_{mix} = \Delta H_{mix} - T\Delta S_{mix}, \tag{1}$$

in which ΔH_{mix} is the enthalpy of mixing, T is the temperature, and ΔS_{mix} is the entropy of mixing. The tendency to form multi-element solid-solution phases is likely using the Boltzmann Hypothesis with the entropy of mixing, ΔS_{Conf}, given in Equation 2,

$$\Delta S_{Conf} = -k \ln w = -R \ln \frac{1}{n} = R \ln n, \tag{2}$$

where k is Boltzmann's constant, w is the number of ways of mixing, R is the gas constant, and n is the number of elements [3]. Because there are multiple principal elements, they can be considered solute atoms. Elements with small atomic-size differences are easily interchangeable and able to sit on lattice sites forming solid solutions. Moreover, the enthalpy of mixing of the elements does not favor the formation of compounds [4]. The resulting high entropy of mixing acts to lower the free energy of solution phases. This trend is accompanied by sluggish diffusion due to the difficult cooperation among the migrations of various elements. Coupled with the severe lattice distortions due to multiple solute atoms, diffusion rates are slower in HEAs [3, 6-8]. Thus, simple solid solutions and nanostructures that avoid the problems of difficult analyses and processing are formed [3, 4]. Figure 1 gives an example schematic of an HEA solid solution.
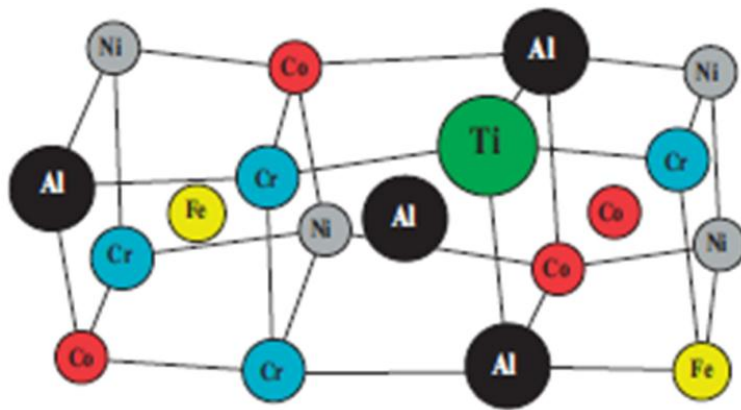
Figure 1. Schematic diagram of a BCC HEA as a solid solution [4].

Furthermore, it has been shown that the valence-electron concentration (VEC) of the constituent elements has an effect on the phase stability [9]. Guo et al. have shown the face-centered cubic (FCC) and body-centered cubic (BCC) phase stabilities of solid solutions, such as HEAs, when the atomic-size ratios are nearly identical [9]. This allows for the possibility of thousands of alloy compositions [3], shown by Equation 3 where C_n^m is the number of combinations of m items taken n times, an exciting development for future alloy design.

$$C_5^{13} + C_6^{13} + C_7^{13} + C_8^{13} + C_9^{13} + C_{10}^{13} + C_{11}^{13} + C_{12}^{13} + C_{13}^{13} = 7099 \tag{3}$$

Generally, HEAs can be defined as being composed of five or more elements in equimolar ratios or near equimolar ratios and can be extended to those compositions in which each principal element concentration is between 5 and 35 atomic percent (at.%) [3]. The mechanical properties of many HEAs have been tested and shown that these alloys may have the potential for use in a wide range of applications, such as those requiring high-temperature strengths, high tensile strengths, increased wear resistance, and corrosion resistance [3, 10-13].

1.2   Mechanical Properties of High-Entropy Alloys

The mechanical properties of many HEA systems have been investigated due to the promising nature of these alloys for use in structural applications. It has been observed that many alloys are sensitive to compositional effects which have a tremendous effect on the microstructure and mechanical properties [3-5, 7, 9, 12, 14-17]. One promising HEA system in particular is the $Al_xCoCrCuFeNi$ system which shows a gradual change from FCC to BCC structures, accompanied by a large increase in hardness, shown in Figure 2, as the aluminum content increases from x = 0 to 2.0 [16]. Compositions, such as $Al_{0.5}CoCrCuFeNi$, show a good combination of strength and ductility at room temperature with a compressive strength higher than 1,380 MPa with a compressive elongation of more than 51.5% [18].
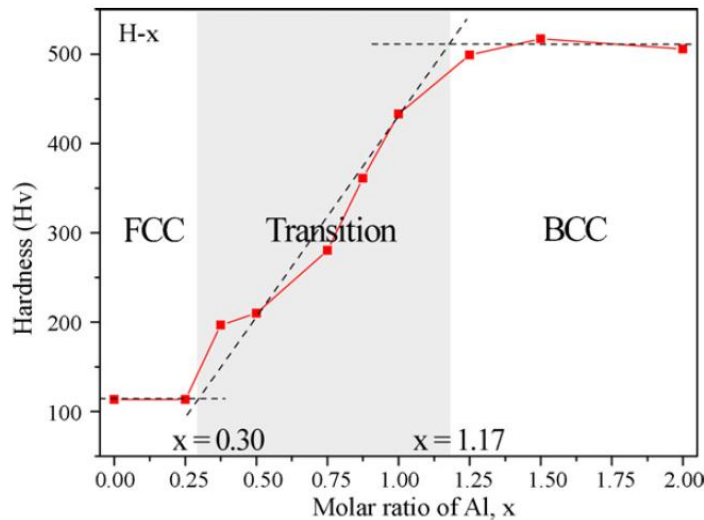
Figure 2. Hardness as a function of Al concentration in the $Al_xCoCrCuFeNi$ HEA system [19].

In order to reliably control the properties of the $Al_xCrCuFeMnNi$ alloy system, and develop it for practical applications, it is essential to better understand all aspects of the microstructures. There is generally a trade-off between strength and ductility in alloy systems, with ductility decreasing as strength increases. In the HEA system of $Al_xCoCrCuFeNi$, strength (hardness) clearly increases as a function of the aluminum concentration (Figure 2). The trend for ductility, however, needs further investigations. An increase in the amount of the BCC phases present compared to the amount of FCC phases reduces the ductility. This is to be expected due to the reduced number of slip systems activated at a particular stress in a BCC systems compared to FCC systems seen in many materials [20].

Studies of HEAs have also been performed at elevated temperatures. It is theorized that, due to high mixing entropy, these alloys will have excellent stability at high temperatures since entropy scales with temperature (Eq. 1). Studies of $Al_xCoCrCuFeNi$, shown in Figure 3, have identified optimal compositions, such as $Al_{0.5}CoCrCuFeNi$, as good candidates for high-temperature applications, up to 800 °C [17, 21]. This conclusion was based, in large part, on a good balance between strength and ductility.
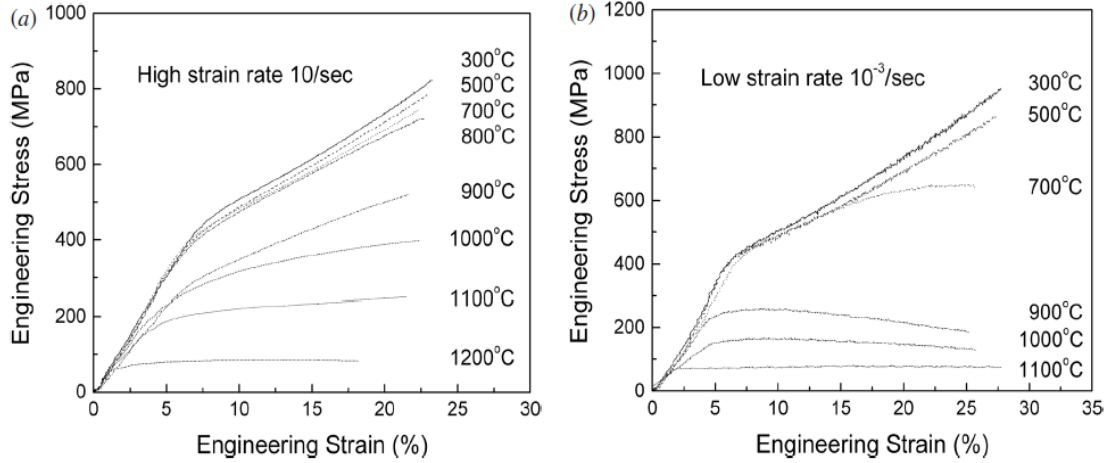
Figure 3. Compressive stress-strain curves of $Al_{0.5}CoCrCuFeNi$ at various temperatures [17].

More recent investigations [22], however, have raised questions about the intermediate temperature embrittlement, between 300 °C and 600 °C, in this HEA due to intermediate phase formation. Controlling this can lead to excellent age-hardening properties and more investigation is need on this front.

The $Al_xCrCuFeMnNi$ system is another such alloy that displays encouraging results for high-temperature applications [23, 24]. These alloys have been shown to have a mix of face-centered cubic (FCC) and body-centered cubic (BCC) phases depending on the aluminum content shown in Figure 4. It is observed that Mn is a BCC stabilizer, promoting the formation of a BCC phase leading to increased hardness in these alloys compared to Co-containing HEAs, shown in Figure 5.
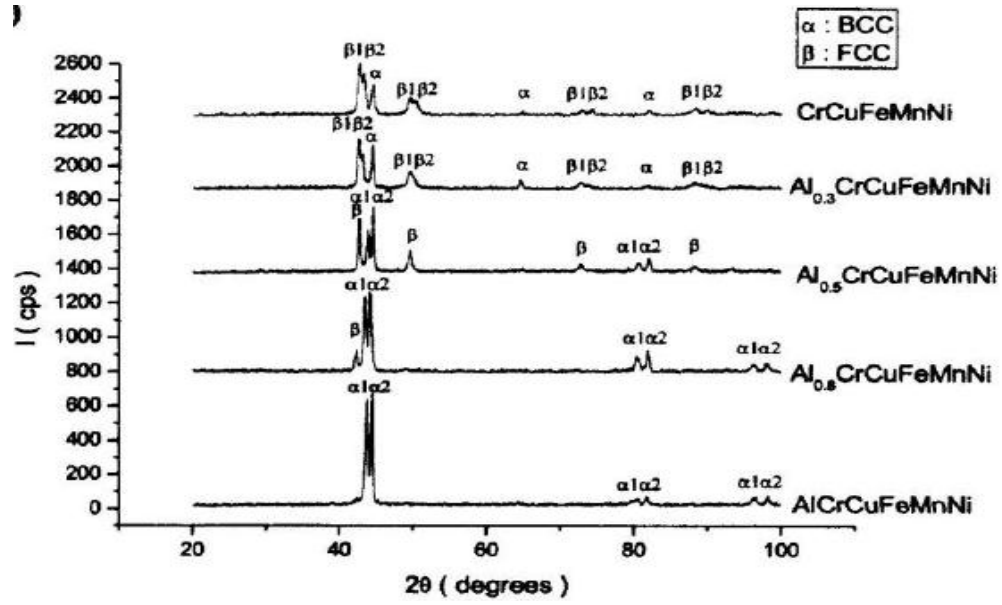
Figure 4. X-ray diffraction patterns of as-cast Al$_x$CrCuFeMnNi HEAs showing the presence of FCC and BCC phases.
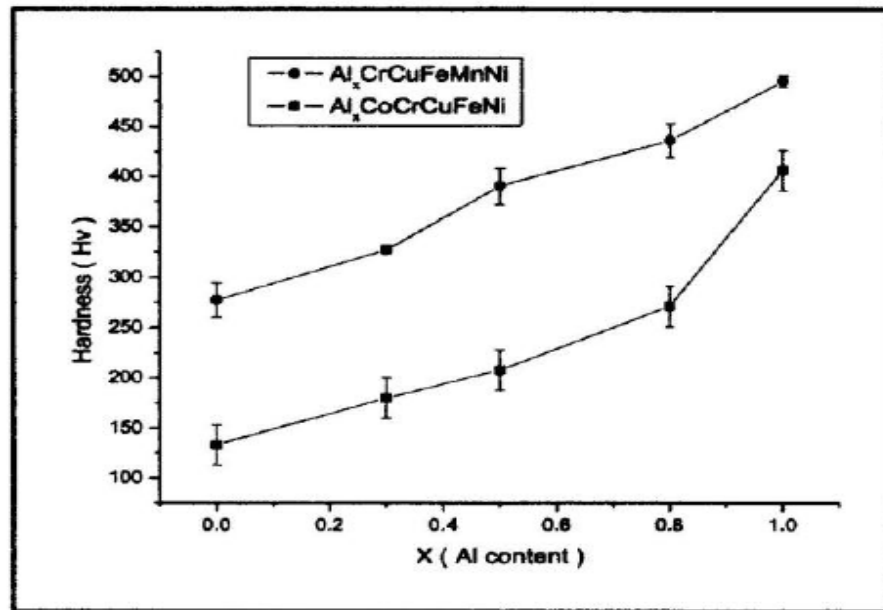
Figure 5. Hardness of Al$_x$CoCrCuFeNi and Al$_x$CrCuFeMnNi with varying Al content.

The elevated-temperature properties of these alloys show encouraging results. Figure 6 presents an age hardening effect seen in these HEAs. An increase in hardness is seen as a result of aging time at 800 °C [23]. As the alloying content is changed the aging properties become more pronounced at different temperatures. For a $Al_{0.5}CrCuFe_{1.5}MnNi_{0.5}$ alloys there is an increase in the hardness from 397 HV to 840 HV after 50 hours of aging at 700 °C [24]. This has been attributed to the formation of a $Cr_5Fe_6Mn_8$ phase which has extremely high hardness (1,273 HV).
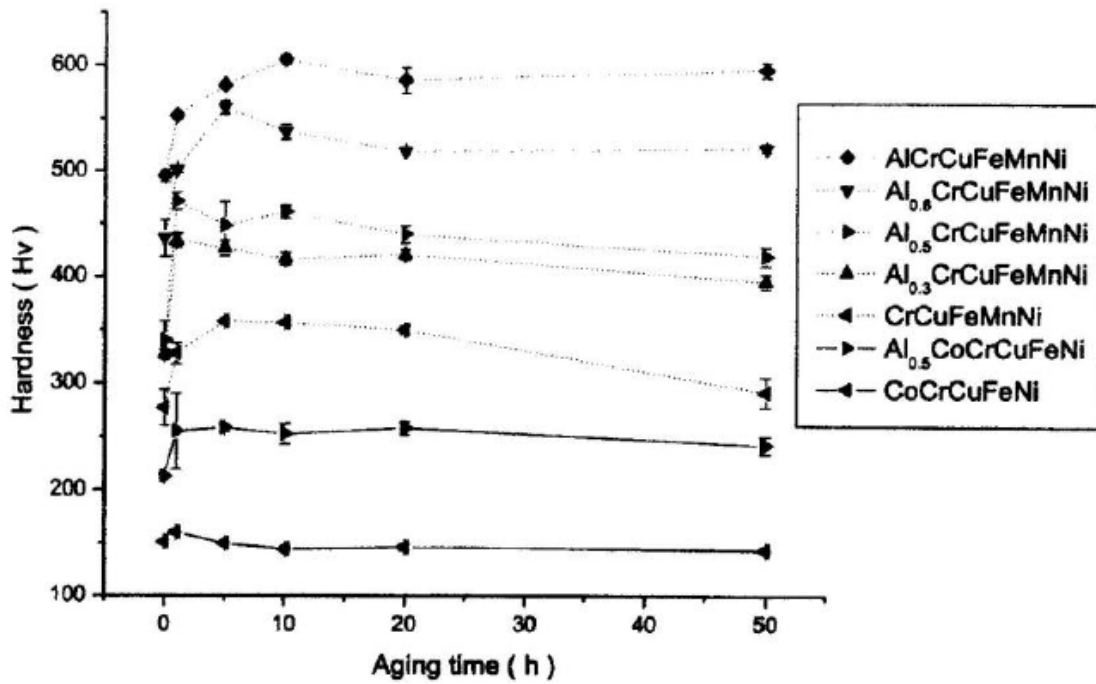
Figure 6. The age hardening of $Al_xCoCrCuFeNi$ (solid line) and $Al_xCrCuFeMnNi$ (dashed line) [23].

HEAs composed of refractory elements have shown even better high-temperature properties and compare favorably with conventional superalloys [10, 11]. Figure 7 shows a comparison of the yield strength as a function of temperature of NbMoTaW and VNbMoTaW HEAs compared to conventional Ni-superalloys. At room temperature these alloys showed high yield strengths of 1,058 MPa and 1,246 MPa, respectively. However, these alloys showed little ductility (< 2.0%) at room temperature suggesting that the ductile to brittle transition temperature of these alloys is somewhere between room-temperature and 600 °C. These alloys have BCC structures that remain stable to temperatures greater than 1,400 °C and have an increased resistance to elevated temperature deformation attributed to the sluggish diffusion in these alloys.
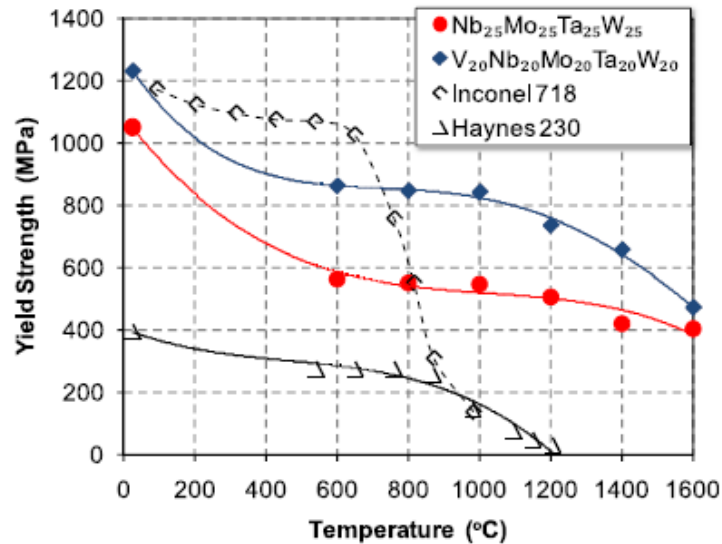
Figure 7. Temperature dependence of the yield strength of two HEAs compared to conventional Ni-superalloys [11].

9

It is seen that many of HEAs have complicated deformation mechanisms attributed to the structure of these alloys. A study of the deformation behavior of the $Al_{0.5}CoCrCuFeNi$ system shows that this can be attributed to low stacking fault energy, solution hardening, elemental segregation, and sluggish diffusion [25]. HEAs tend to show strong work hardening particularly after cold rolling due to the presence of a large amount of nano-twins. This deformation mechanism is attributed to the Suzuki interaction where the stacking fault energy is lowered and, thus, a separation in the distance of partial dislocations is seen. This favors twinning due to the lower critical stress required to nucleate twins compared to dislocations.

Additionally, lattice distortion from the solid solution increases the strength of the matrix raising the critical stress to move dislocations [20, 25]. Dislocation motion is also inhibited by second phase precipitates that have formed due to elemental segregation, i.e. copper-rich particles. This further reduction in dislocation mobility causes twinning to be activated more easily. Increased deformation leads to an increase in the twin density. The formation of additional twins requires a further increase in stress. Thus, HEAs show excellent work hardening and increased strengths.

1.3   Fatigue Behavior of Structural Alloys

Structural materials are used in a wide variety of operating conditions and rarely are they subjected to constant, static loads. Most components experience some type of variable loading conditions through their lifetime. Dynamic loading conditions are known to cause failure over time in components at lower stresses than the stress required to cause failure with a single application of a load. Failures due to repeated loads over a period of time are referred to as fatigue failures [20, 26-29]. Due to the sheer number of components subjected to fatigue conditions and the difficulty in detecting any deterioration in performance (if any) under these conditions, it is estimated that almost 90% of all mechanical failures that occur during service can be attributed to fatigue [20, 27]. Clearly, understanding the fatigue behavior of a new class of structural alloys is imperative if these alloys are to have practical applications in industry.

1.3.1 Fatigue Terms

It will be useful, then, to describe some common terms used to describe fatigue behavior. Many applications are only concerned about the fatigue behavior at a very high number of cycles ($> 10^5$) called high-cycle fatigue. Here, deformation is macroscopically elastic and failure occurs due to localized plastic buildup. Low-cycle fatigue is another type of fatigue that occurs at $N < 10^5$ cycles and is characterized by controlling the strain into the plastic regime. This study will only be concerned with high-cycle fatigue. However, due to the numerous

potential applications for HEAs at elevated temperatures, it is the author's opinion that, in the future, this could be an interesting area of investigation to characterize how HEAs behave during thermal fluctuations and other similar processes.

High-cycle fatigue data is normally presented in S-N plots, i.e. the stress (S) versus the number of cycles to failure (N), also called the fatigue life. The fatigue life is determined when complete fracture has occurred, unless otherwise stated. An example of a typical S-N curve for steel and aluminum can be seen in Figure 8. Generally, at higher stresses shorter fatigue lives are observed compared to lower stress where longer fatigue lives are seen. Some materials, such as some steel and titanium alloys, show a sharp change in the curve to horizontal at a particular stress. This is referred to as the fatigue endurance limit meaning a component ran at an applied stress below the endurance limit will, presumably, never fail. This is seen in Figure 8 for the mild steel. Most materials see a steady increase in the fatigue life as the stress decreases but eventually failure occurs at some point. This trend is seen in Figure 8 for the aluminum alloy. In these cases a material is given a fatigue strength depending on a specified number of cycles, i.e. the fatigue life at 10^6 or 10^7 cycles.
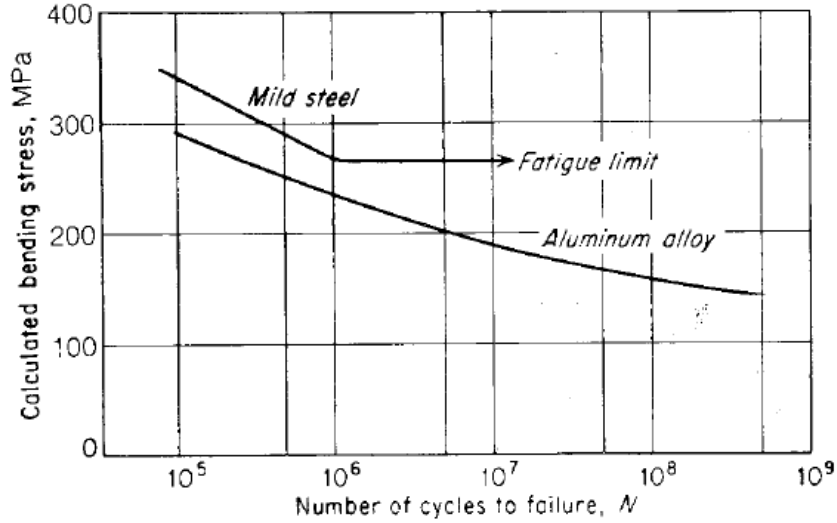
Figure 8. Typical S-N curve for steel and aluminum alloy illustrating the fatigue life and endurance limit [20].

It is important to characterize the type of alternating stress that can cause fatigue in components. Stress fluctuates from a maximum, σ_{max}, to a minimum, σ_{min}, in repeated cycles, usually in a regular pattern. An example stress cycle can be seen in Figure 9. Two components can then characterize the stress cycle, a mean stress, σ_m, also called the steady state stress, and an alternating stress, σ_a. The algebraic difference in the maximum stress and minimum stress is referred to as the stress range, σ_r. Materials are sensitive to all components of the stress and may behave differently if the parameters are changed, for instance, under completely reversed stress (tension and compression) as opposed to repeated tensile stress. For this reason it is customary to indicate the parameters of test such as the stress ratio given in Equation 4.

$$R = \frac{\sigma_{min}}{\sigma_{max}} \tag{4}$$
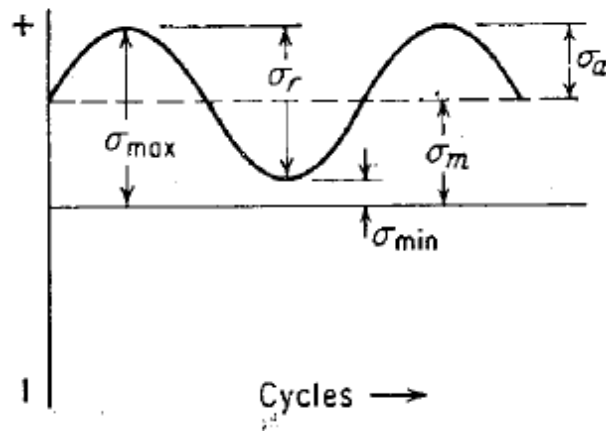
Figure 9. Typical repeated stress fatigue cycle [20].

1.3.2 Fatigue Failure

The fatigue behavior can be divided into three major stages, crack initiation, crack growth, and final failure. There are many theories to the actual mechanisms of crack initiation although it is still not fully understood [20, 26-28]. In general, crack initiation begins at the surface due to the buildup of local plastic deformation. It is well know that the surface conditions play a major role in the fatigue behavior. The surface is much more likely to contain stress concentrators such as notches and bending and twisting moments. Further, second phase particles with different elastic and plastic properties may serve as stress concentrators. At these points it is common to see a buildup of slip bands leading to the formation of microcracks.

The initial formation of microcracks begins very early in the total fatigue life. Some of these begin to grow but very few additional cracks are formed late in the fatigue life of components. Once formed they initially propagate along

14

specific slip planes until later in the growth when they usually begin propagating in a direction perpendicular to the maximum applied stress. This stage of crack growth is the most apparent when observing the fracture surface. Whereas crack initiation and initial growth along slip bands is very small, in this stage, indications of the crack propagation are easily seen. At each successive cycle there is a maximum and minimum stress applied at the crack tip causing localized plastic deformation. As the crack advances a ripple pattern, known as striations, can be seen advancing due to the opening and closing of the crack tip. Each striation is an indication of one stress cycle. Eventually the crack or cracks will propagate to such a length that the remaining cross sectional area is insufficient to support the applied stress and final failure will occur.

1.3.3 Statistical Nature of Fatigue

It is obvious that crack initiation is sensitive to even the smallest of imperfections. This can lead to considerable differences in the measured fatigue lives at similar stresses and, thus, considerable scatter in fatigue test data. Often, specimens are seen to fail at lives much lower than predicted mean fatigue lifetimes and it is usually observed that as the stress increases the scatter will reduce. As such, it is usually necessary to consider fatigue data as a statistical quantity or the probability that a specimen will achieve a particular lifetime. Many models have been used to characterize the statistical nature of fatigue including Gaussian distributions. This study will utilize a Weibull distribution to characterize the scatter in the measured fatigue data.

CHAPTER 2
Fatigue Behavior of $Al_9Co_{18.2}Cr_{18.2}Cu_{18.2}Fe_{18.2}Ni_{18.2}$ and $Al_{7.5}Cr_{22.5}Fe_{35}Mn_{20}Ni_{15}$ HEAs

2.1   Introduction

This investigation will study the fatigue behavior of the $Al_9Co_{18.2}Cr_{18.2}Cu_{18.2}Fe_{18.2}Ni_{18.2}$ and $Al_{7.5}Cr_{22.5}Fe_{35}Mn_{20}Ni_{15}$ (atomic %) HEAs. For the sake of simplicity the $Al_9Co_{18.2}Cr_{18.2}Cu_{18.2}Fe_{18.2}Ni_{18.2}$ system may be written as $Al_{0.5}CoCrCuFeNi$ (atomic ratio) or referred to as FCC-HEAs. The $Al_{7.5}Cr_{22.5}Fe_{35}Mn_{20}Ni_{15}$ system may be referred to as BCC-HEAs. Structural characterizations of the $Al_{0.5}CoCrCuFeNi$ alloy show two distinct phases, a main α-FCC phase and a copper-rich β-FCC phase [7, 30]. Both show similar lattice constants of about 3.6 Å [7]. In the homogenized and water-quenched condition, both phases are in a supersaturated state and exhibit aging hardening between 300 and 700 °C due to the precipitation of Al- and Ni-rich BCC phases [22]. This precipitation-hardening feature increases the strength but is accompanied by a loss in the ductility. In the as-rolled and as-annealed (at 900 °C) condition, the $Al_{0.5}CoCrCuFeNi$ HEA displays a better combination of strength and ductility, as compared to conventional alloys, such as 304 stainless steel and Ti-6Al-4V titanium alloy [22].

The $Al_{7.5}Cr_{22.5}Fe_{35}Mn_{20}Ni_{15}$ system is has been studied as an alternative to the Al-Co-Cr-Cu-Fe-Ni system. First, it seeks to lower the cost of the raw materials by substituting the much more expensive and strategic element Co with Mn. Second, it removes Cu to remove the effect of Cu segregation to

interdendrite regions [24]. X-ray diffraction of this alloys shows it has a mixture of an FCC and BCC structure with lattice constants of 3.63 Å and 2.88 Å, respectively [24]. An increase in the amount of Al in system is seen to promote the formation of a fully BCC structure consistent with other HEAs upon the addition of aluminum [7, 24]. The microstructure of these alloys shows two distinct phases with a dendrite BCC phase and interdendrite FCC phase. It has been observed and described in Chapter 1 that Al and Cr are BCC stabilizers which is consistent with ferrous alloys and confirming that the dendrite phase is indeed the BCC phase [24, 31]. This phase has a fine dispersion of solution B2-type Ni-Al particles. This alloys shows significant age hardening from 600 – 800 °C due to the formation of the ρ-$Cr_5Fe_6Mn_8$ phase.

The mechanical properties of the as-cast $Al_xCoCrCuFeNi$ (x = 0 ~ 3 at. ratio) alloys are readily available and described in Chapter 1 [17]. However, little research has been performed on the $Al_{7.5}Cr_{22.5}Fe_{35}Mn_{20}Ni_{15}$ system and no research, the best of the author's knowledge, has been conducted to investigate the fatigue behavior of these and other promising HEA systems [3, 10-13, 17, 30, 32, 33]. This chapter will examine the mechanical properties and fatigue behavior of $Al_{0.5}CoCrCuFeNi$ FCC-HEAs and $Al_{7.5}Cr_{22.5}Fe_{35}Mn_{20}Ni_{15}$ BCC-HEAs. Statistical modeling using a Weibull distribution will be conducted to further investigate the fatigue characteristics of the FCC-HEA and discussed in Chapter 3. Chapter 4 will be a discussion of fatigue behavior and a comparison of HEAs to other conventional materials.

2.2   Experimental Procedure

The samples of both $Al_{0.5}CoCrCuFeNi$ and $Al_{7.5}Cr_{22.5}Fe_{35}Mn_{20}Ni_{15}$ HEAs were prepared by arc-melting the constituent elements with a current of 500 amps in a water-cooled, copper hearth. The elements were all at least 99 weight percent pure, and the melting was accomplished in a vacuum of at least 0.01 torr. The melting and solidification processes were repeated at least five times to improve the chemical homogeneity of the sample. The FCC-HEA cast samples were annealed at 1,000 °C for six hours, water quenched, and cold rolled. The rolling reduction was 84% with a final thickness of 3 mm. The BCC-HEAs were forged to a thickness of 5 mm at 1,000 °C and held at this temperature for 30 min then water quenched. The slab was then rolled at 350 °C to a final thickness of 3 mm for a total of a 40% reduction in thickness.

The rolled sheets of both alloys were, subsequently, machined into fatigue samples with dimensions of 25 mm x 3 mm x 3 mm for four-point-bend fatigue experiments, as described below. Samples were machined parallel to the rolling direction. That is, the 25-mm length of the samples runs parallel to the rolling direction. Thus, the applied stress on the tensile edge will be parallel to the rolling direction. Two distinct microstructures were observed in this region (and in the samples as a whole) depending on the sample's position in the mold during casting, as discussed later in the experimental results. Hence, the fatigue behavior as a function of the characteristic microstructure was also determined.

To remove as many surface imperfections as possible, the samples were polished on a Buheler rotating grinder and polisher. Grits of 240, 400, 600, and

1,200 were used in the respective order. The sample was turned 90° after each polishing step finishing with the 1,200 grit running parallel along the length direction of the sample so as not to introduce scratches that could act as small notches perpendicular to stress.

Tensile and compression experiments were performed on samples of the as-rolled FCC-HEAs and BCC-HEAs, respectively, to characterize the mechanical behavior of the alloys, and their results are used to compare to other conventional alloys. The gauge section of the FCC-HEA tensile specimens was machined to a size of 3 mm x 12 mm and tested on an Instron 4505 at a strain rate of 1×10^{-3} s^{-1}. The specimens were tested to failure to determine the yield strength, ultimate tensile strength, and the percent elongation. Compression tests were performed on the BCC-HEAs using a Materials Test System (MTS) servohydraulic machine at a strain rate of 1×10^{-3} s^{-1} on samples with a length to diameter ratio (L/D) of 2. The strain was measured with MTS Extensometer.

To study the fatigue behavior of the HEA samples, four-point-bend tests were conducted at various applied loads and ran until the failure of the specimen or 10^{7} cycles was reached. The results of the fatigue tests were plotted on a typical S-N curve. The maximum stress, σ, on the tensile surface within the span of the two outer pins in the four-point-bend fatigue experiment was calculated, using the following beam-theory relationship [34],

$$\sigma = \frac{3P(S_o - S_i)}{2BW^2}$$

(5)

where P is the applied load, S_o is the outer span length of 20 mm, S_i is the inner span length of 10 mm, B is the thickness, and W is the height. In this investigation, $B \approx W \approx 3$ mm. Images of the experimental setup and a schematic of the four-point-bend test can be seen in Figure 8. The samples were tested at 10 Hz with a loading ratio of $R = \sigma_{min.} / \sigma_{max.} = 0.1$ [34].

High-energy x-ray diffraction (XRD) was performed on FCC-HEAs at the Advanced Photon Source (APS) using the 11-ID beamline located at the Argonne National Laboratory to obtain diffraction patterns of the sample for structural characterizations. The specimens were 1 mm thick using a beam energy of 115.27 keV. The scattered, transmitted x-rays were collected using a Mar345 image plate [35].

Microstructural features of the tensile regions of the fatigue samples were analyzed, using back-scattered electron microscopy (BSE) to determine the homogeneity of the microstructures. The fracture surfaces were investigated to study the fatigue mechanisms using scanning-electron microscopy (SEM). The BSE, SEM, and energy-dispersive x-ray spectroscopy (EDS) for microstructural characterizations were performed with a Gemini Leo 1525 scanning-electron microscope at 15 kV and 20 kV.
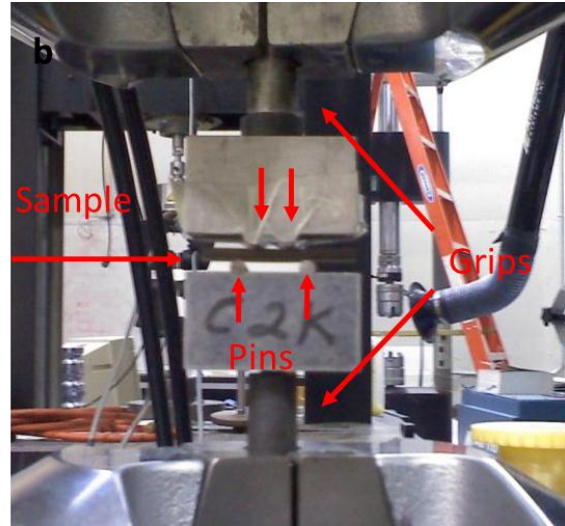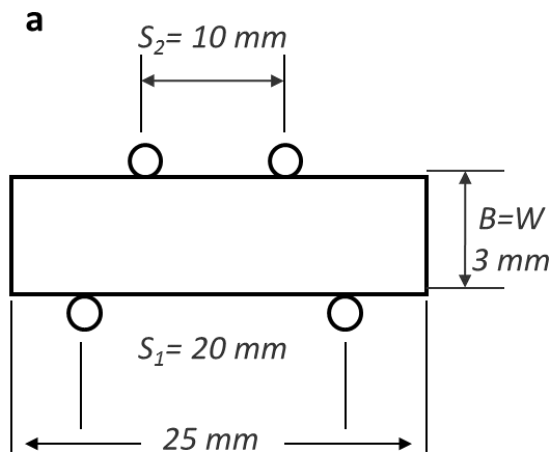
Figure 10. a) Schematic of the four-point-bend setup to show dimensions and b) experimental test setup.

2.3 Experimental Results

Tension tests were initially performed on the FCC-HEAs to characterize the mechanical behavior of the rolled material. The results are shown in Figure 11. The specimen exhibits a high yield stress of 1,284 MPa and ultimate tensile strength (UTS) of 1,344 MPa, generally, exceeding that of conventional alloys, such as steels, titanium, aluminum, and nickel alloys [27, 36-38]. Advanced alloys, such as bulk metallic glasses (BMGs), usually have higher strengths and lack tensile ductility. However, the present FCC-HEA shows a degree of plastic deformation necessary in structural applications with a tensile elongation of 7.6% for the as-rolled material.

Compression of BCC-HEA is shown in Figure 12. This alloy has a yield stress of 1,254 MPa and displays significant strain hardening to 2,580 MPa. This alloy also shows sufficient ductility for structural applications with an elongation of 15% before the test was stopped. Again, these values of strength and ductility compare favorably to many conventional alloys.

Hardness testing was also conducted on both samples. The FCC-HEAs had an average hardness of 378.8 ± 27 HV. This agrees very well with the reported literature value 378 ± 12HV [25]. BCC-HEAs had a hardness of 390.3 ± 14 HV which is also in good agreement with the reported literature value of 386 ± 7 HV [24]. The high hardness of these samples compared to as-cast samples [17] is due significant work hardening from the rolling operation. Even after undergoing homogenization at 1,000 °C recovery is slow due to the reduced diffusion of HEAs [7, 25].
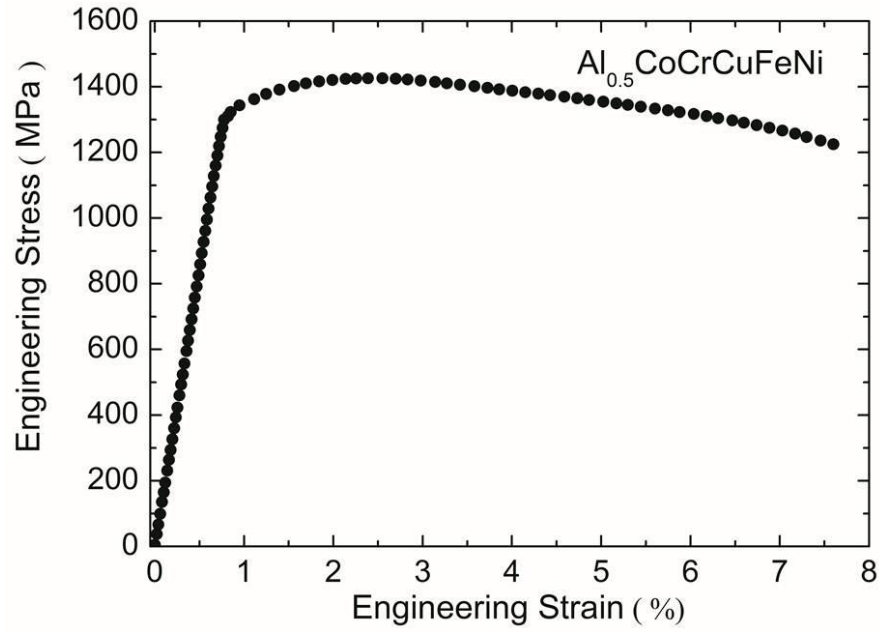
Figure 11. Engineering stress vs. strain curve of the $Al_{0.5}CoCrCuFeNi$ HEA under tension at room-temperature and a strain rate of 10^{-3} s^{-1}.
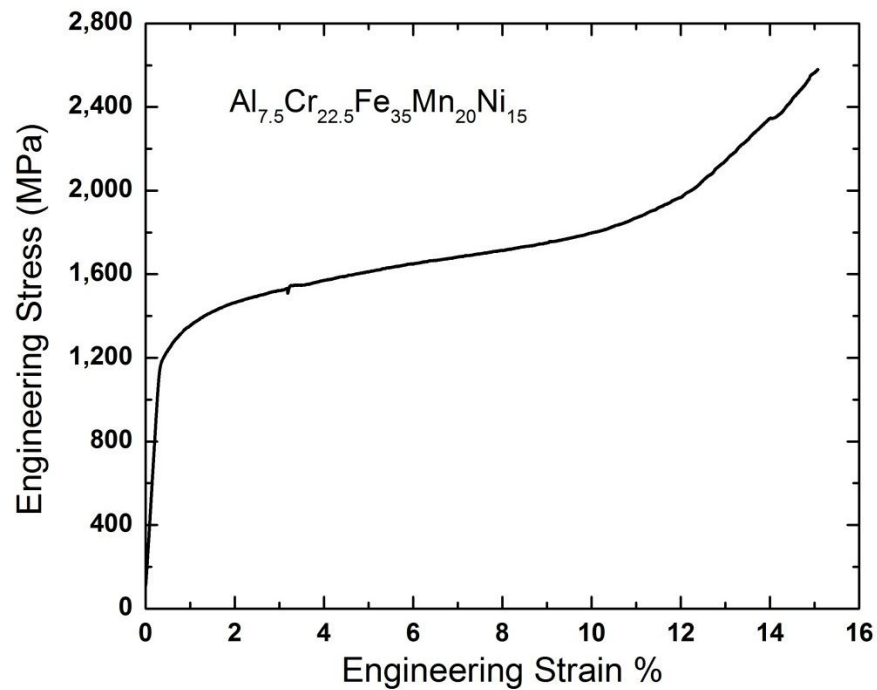
Figure 12. Engineering stress vs. strain curve of the BCC-HEA under compression at room-temperature and a strain rate of 10^{-3} s^{-1}.

23

Microstructural characterizations were performed on FCC-HEAs using synchrotron XRD and SEM. Figure 13 shows a synchrotron XRD pattern of the $Al_{0.5}CoCrCuFeNi$ HEA and averaged at azimuthal angles (φ) between 55 and 65 degrees. The pattern indicates an FCC structure with the presence of some ordered structure indicated by the 100 peak. This ordered structure is the L12 phase, similar to the Ni_3Al intermetallic compound, homogeneously dispersed in the FCC matrix as observed previously by transmission-electron microscopy (TEM) analyses [7, 39]. The low peak intensity can be partially attributed to the high amount of lattice strains present in the alloy [7]. The lower heights of the (111) and (220) peaks relative to the (200), (311), and (400) peaks are due to the texture in the sample introduced in the rolling deformation. Detection limits of XRD to approximately 1 volume percent have masked the detection of any minor phases, such as oxide particles, later shown to be present by the EDS analyses. Only one set of FCC peaks is seen in the XRD pattern. Previous studies have shown that the lattice constants of these two phases are very similar, approximately 3.6Å [7]. This trend will cause the overlapping of the characteristic diffraction peaks if the resolution of the experimental setup is not high enough. It is important to note that because no BCC characteristic peaks were observed, the structure is indeed a two-phase FCC structure.
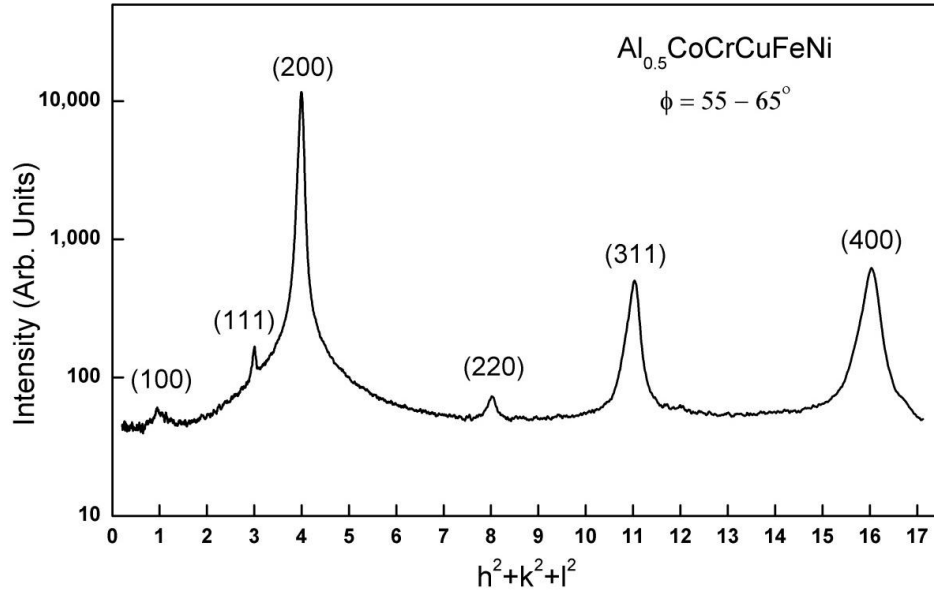
Figure 13. Diffraction pattern of the $Al_{0.5}CoCrCuFeNi$ HEA specimen using synchrotron high-energy x-rays.

BSE and EDS analyses of the specimens were performed to observe and determine the elemental compositions of the specimens. Figure 14 shows an SEM micrograph of a typical sample. The microstructure consists of two phases: the α-FCC matrix phase formed from the FCC dendrite phase (the dark phase) and the β-FCC Cu-rich phase (the light phase) developed from the FCC Cu-rich interdendritic phase. The Cu-rich phase is seen to elongate along the rolling direction [22]. The elemental compositions of these two phases are shown in Table 1. It is observed that the Cu-rich phase has a Cu content of 59 atomic percent (at.%). This phase separation is due to the relatively large positive bonding energies of Cu-Fe, Cu-Co, and Cu-Cr due to copper's tendency to segregate in clusters [7, 39].

25
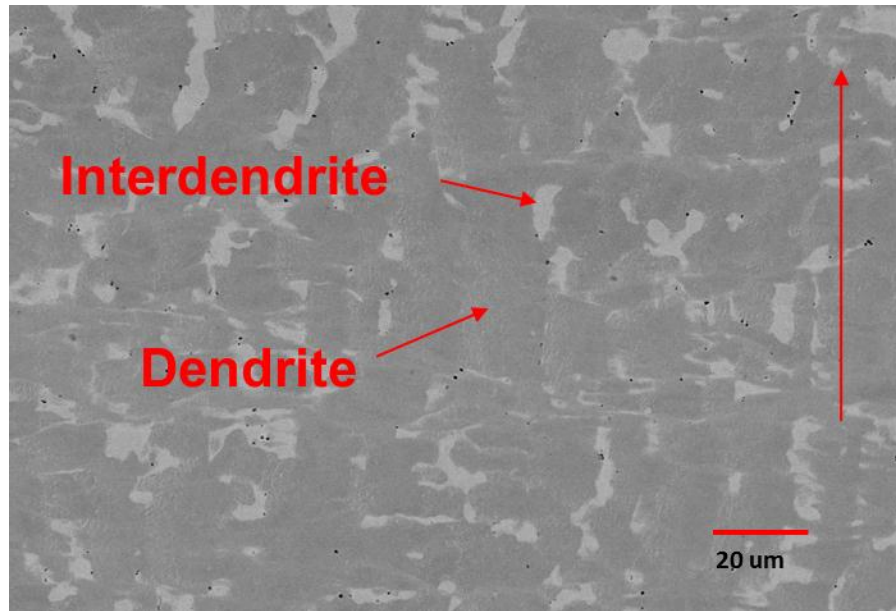
Figure 14. SEM micrograph showing the α-FCC matrix dendrite phase and β-Cu-rich FCC interdendritic phase elongated along the rolling direction indicated by the arrow.

Table 1. EDS analyses of the matrix (dendrite) and Cu-rich (interdendrite) phases in the microstructures of the $Al_{0.5}CoCrCuFeNi$ HEA.

$Al_{0.5}CoCrCuFeNi$ Phase Compositions (Atomic %)						
Region	Al	Co	Cr	Cu	Fe	Ni
Dendrite Matrix phase	7	20	21	11	22	18
Interdendrite Cu-rich phase	10	5	4	59	6	15

Four-point-bend fatigue tests were performed, and the results plotted by the stress range (the maximum stress calculated from Equation 5 and the range $(0.9\sigma_{max.})$ determined using R = 0.1) versus the number of cycles to failure or 10^7 cycles to give the S-N curve seen in Figures 15a and 15b. There is a noticeable amount of scatter at various stress levels for the FCC-HEAs. The results do display typical fatigue behavior for crystalline materials corresponding to an increase in the number of cycles to failure, as the stress level decreases.

In Figure 15a, which displays the data for the FCC-HEAs, it is seen that at a stress range of 1,125 MPa, corresponding to a maximum stress of 1,250 MPa near the yield stress of 1,284 MPa, most failures are within an order of magnitude from around 35,000 to 450,000 cycles, although there is still a high amount of scatter. As the stress level decreases, the spread in the data is even more pronounced, which is generally characteristic of fatigue behavior [26]. Estimations of the endurance limits based on the stress ranges were placed with a lower bound of 540 MPa and an upper bound of 945 MPa. Values were chosen because the specimens reached 10^7 cycles without failure.

Figure 15b displays the fatigue data for BCC-HEAs. Again, there is some scatter seen. At a stress range of 630 MPa a specimen failed at less than 10,000 cycles while the other was ran to completion without failure. It is estimated that these alloys have a fatigue limit between 540 and 630 MPa. Figures 15 a and b were combined to show a comparison of the two alloys and shown in Figure 16.
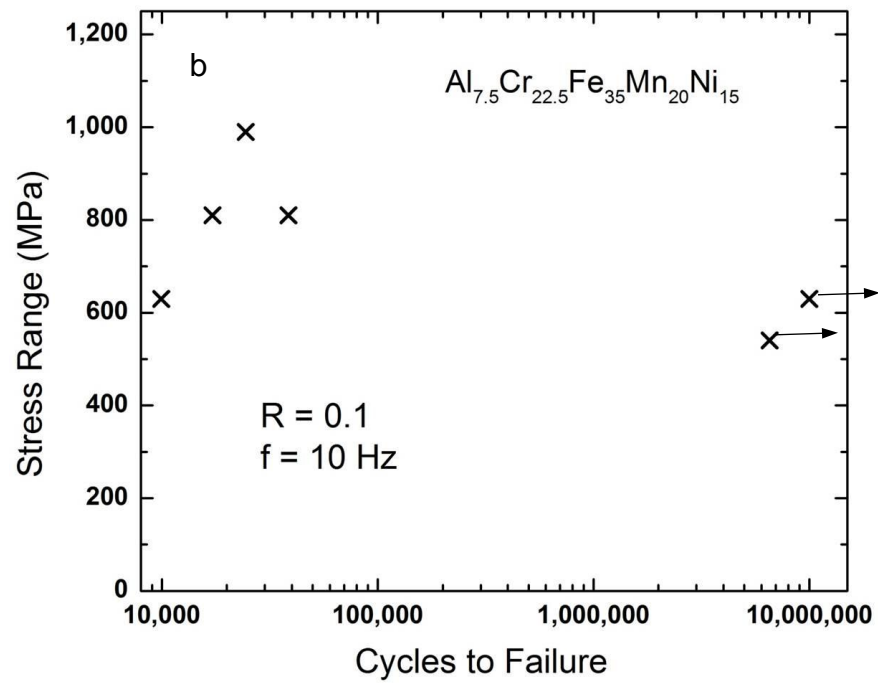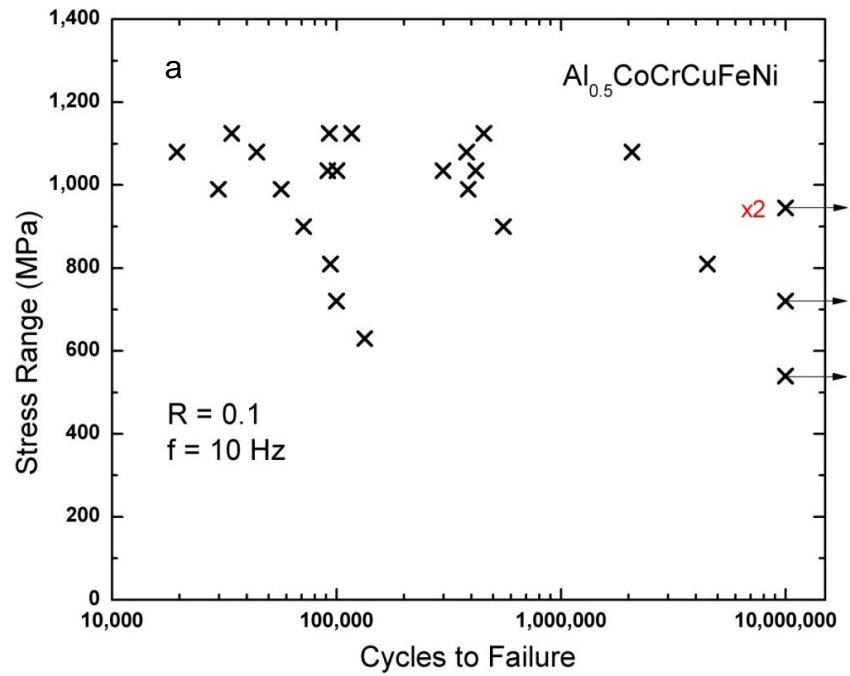
Figure 15. S-N curve for a) the $Al_{0.5}CoCrCuFeNi$ HEA and b) S-N curve for $Al_{7.5}Cr_{22.5}Fe_{35}Mn_{20}Ni_{15}$ HEA plotted with the stress range versus the number of cycles to failure.
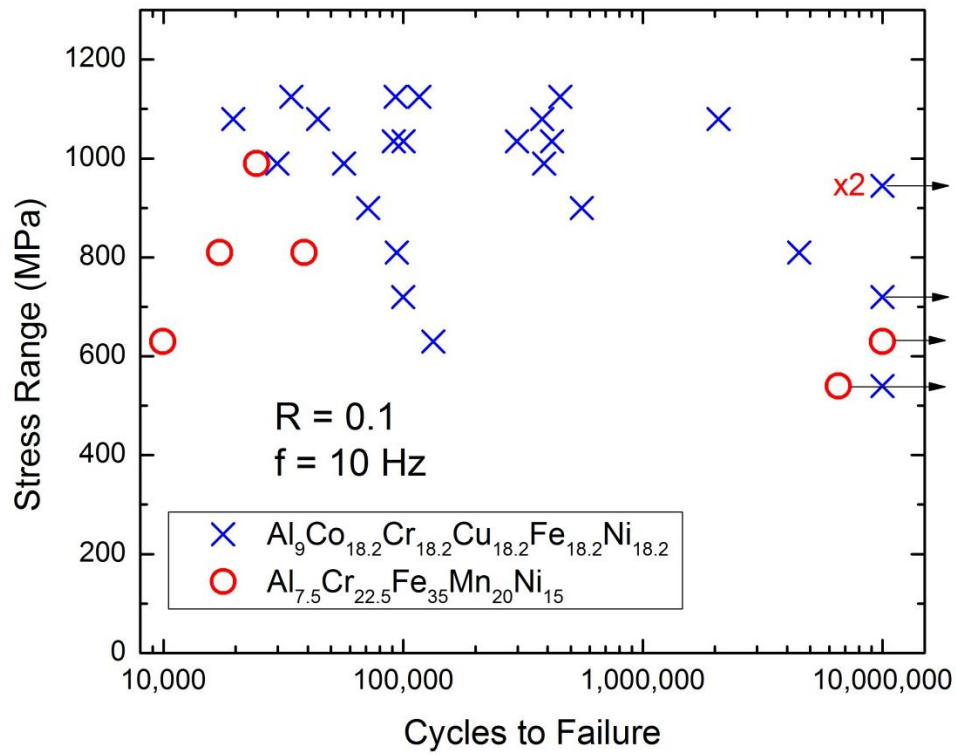
Figure 16. A comparison of the S-N curves for $Al_9Co_{18.2}Cr_{18.2}Cu_{18.2}Fe_{18.2}Ni_{18.2}$ (x symbols) and $Al_{7.5}Cr_{22.5}Fe_{35}Mn_{20}Ni_{15}$ (O symbols) HEAs.

The microstructure morphology was taken into account to try to determine if this feature had an effect on the fatigue life. Although the fatigue specimens were machined in parallel to the rolling direction, the morphology of the matrix phase (α) and the Cu-rich phase (β) in the tensile region of the sample might be different from sample to sample. This trend could be tracked to their position and the different heat-flow directions in the copper mold during solidification. Therefore, the orientation of the loading direction in relation to the different morphologies was investigated.

The SEM micrographs presented in Figure 17 show two typical morphologies observed in the tensile region of the samples. Figure 17a displays the parallel morphology, which features a lamellar flow pattern of alternating α and β phases. Figure 17b presents the vertical type characterized by a random orientation of the α and β phases. After the microstructure identification for all tested samples by SEM, Figure 16 is re-plotted as Figure 18, and shows the fatigue behavior of the parallel and vertical types of samples. It appears that there is no correlation between the scatter in the fatigue life and the orientation of the loading direction with respect to the different morphology, and later statistical modeling efforts confirm this trend. Thus, the orientation and morphology of the phases do not appear to have a significant effect on the fatigue life.
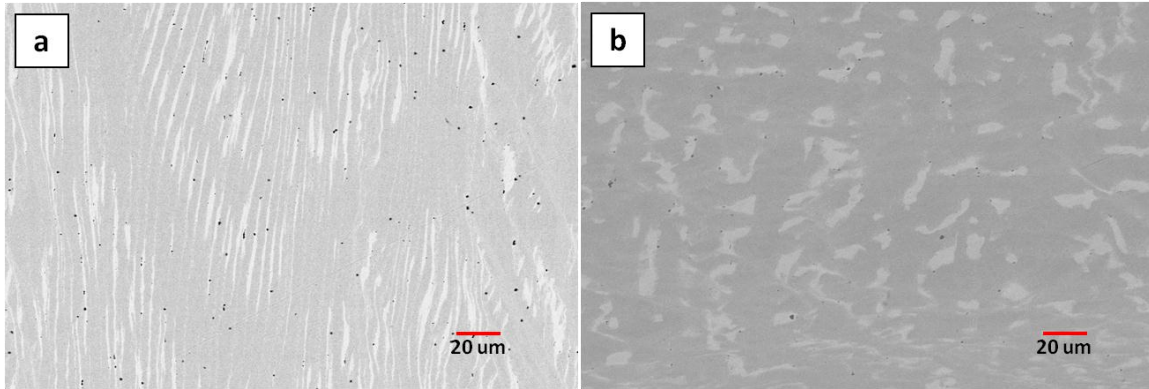
Figure 17. SEM micrographs showing two different types of morphology: (a) the parallel type featured with a lamellar flow pattern of alternating α and β phases and (b) the vertical type featured by a random orientation of α and β phases.
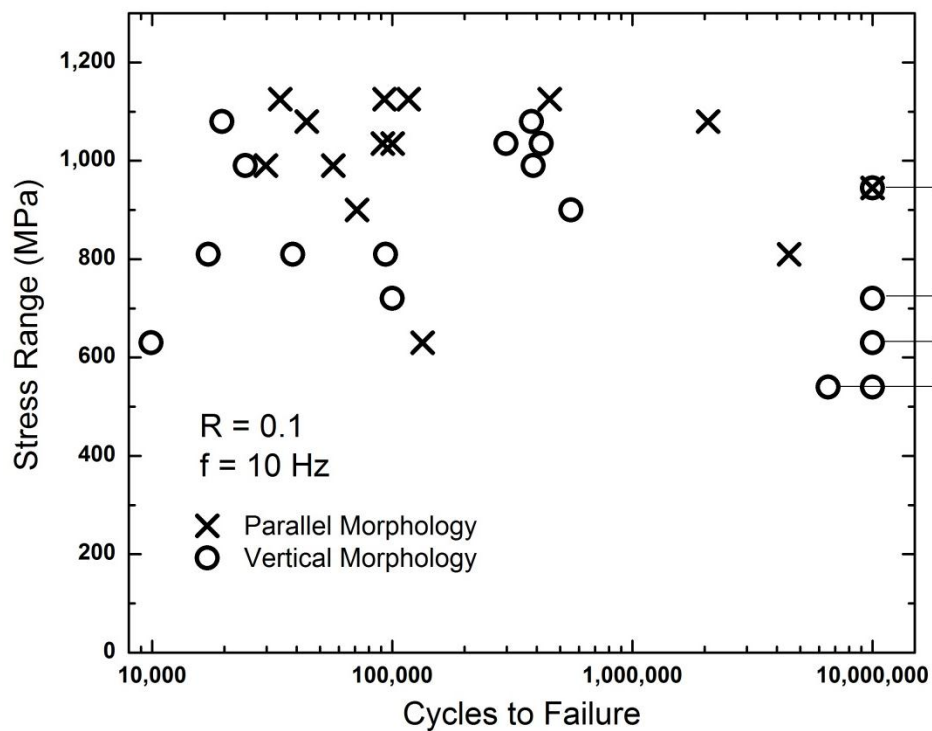
Figure 18. S-N curve presenting scattering of the cycles to failure for the parallel- and vertical-type morphologies in the samples, respectively.

A likely cause for the variable fatigue life is due to the amount of defects in the sample introduced during the casting and rolling processes. In particular, aluminum-oxide-rich particles formed during the melting and solidification process as well as the homogenization process. EDS analyses were performed on these particles to examine their approximate compositions and can be seen in Figure 19. This feature shows the presence of approximately 50% oxygen consistent with aluminum-oxide particles. These particles provide nucleation sites for microcracks due to the stress concentration at the particles.
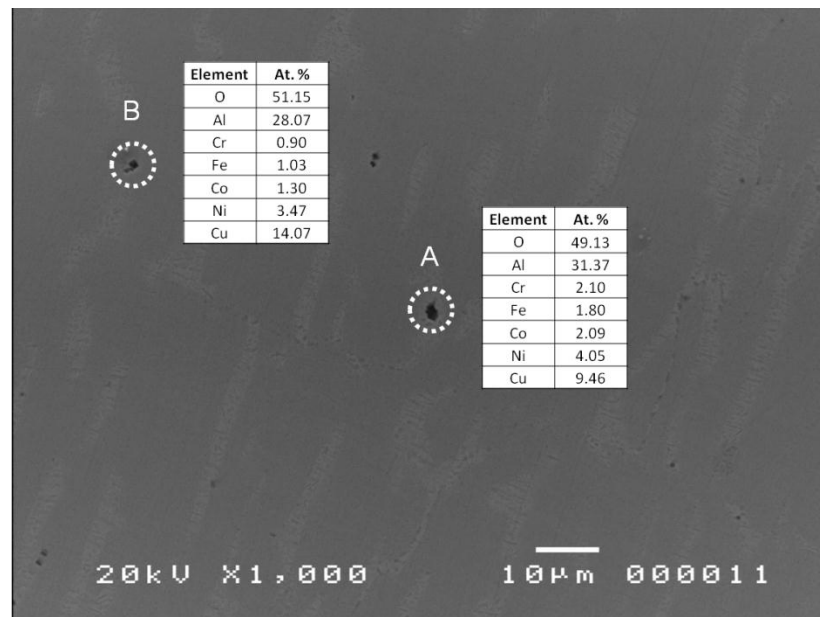
Figure 19. SEM micrograph with EDS analyses of the aluminum-oxide particles. The compositions of the regions labeled A and B are given in the corresponding tables, indicating the presence of aluminum-oxide particles.

Figure 20 presents the number of cycles to failure versus the number of defects per 240 µm x 165 µm observed at 500x magnification in specimens of various stress levels. It can be observed that a decrease in the number of defects may correlate to an increase in the fatigue life at various stress levels. The air-cooled or final solidification side of the casting contains more segregation, inclusions, and shrinkage pores, which could induce microcracks during cold rolling and the initial stages of fatigue. If high densities of these microcracks are located on the tensile side during the four-point-bend fatigue loading, the fatigue resistance would be reduced, and failure would occur after fewer cycles.
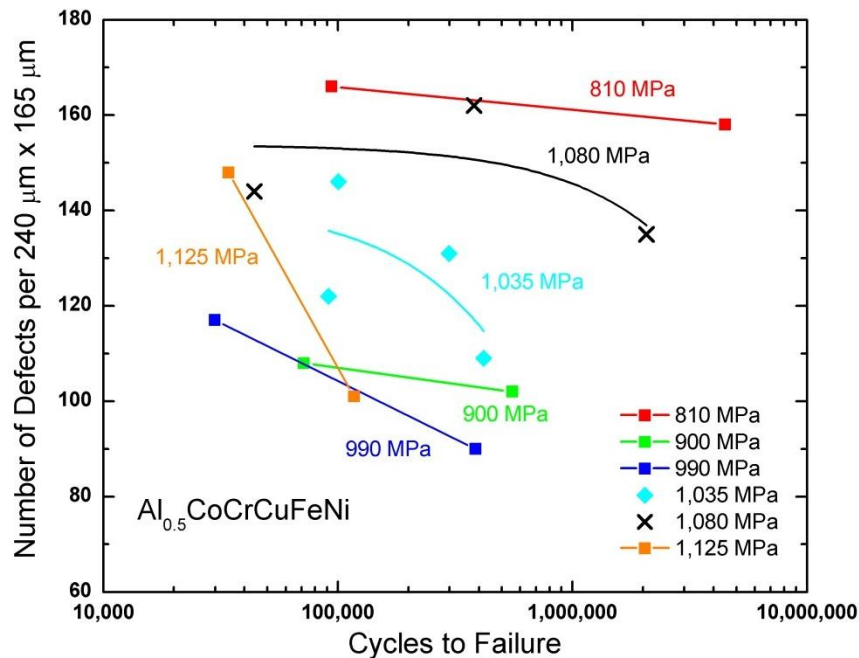
Figure 20. The cycles to failure compared to the number of surface defects at various stress range levels showing that as the number of defects decreases, the life generally increases at a particular maximum stress level.

Fracture surfaces were analyzed to determine the unique fatigue characteristics of the samples, such as crack-initiation sites, propagation, and final fracture and shown in Figures 21 – 24. Figure 21a shows the fracture surface of an FCC-HEA sample that failed at a stress range of 900 MPa after 555,235 cycles. Figure 21b presents the crack-initiation behavior from microcracks that have formed from defects on the surface of this sample. Figures 22a and 22b show a similar phenomenon occurring for BCC-HEAs. This sample was run at a stress range of 990 MPa and failed after 24,460 cycles. Oxides on the surface are apparent and can have sizes on the order of tens of microns. A buildup of slip bands is observed with microcracks nucleating from these.

The samples exhibit similar fracture patterns with crack initiation within the tensile region of the sample surface. Cracks usually initiated at defects present on the surface, as discussed later, or at the corner of the samples. Inclusions on the surface of the FCC-HEAs were usually much smaller than those observed for BCC-HEAs. These areas represent high stress-concentration regions favorable for crack nucleation.

Numerous cracks nucleate and grow perpendicular to the stress in the specimen (parallel to the applied load) through the tensile region. For the FCC-HEAs crack propagation generally occurs through approximately one third of the cross section before the final failure, depending on the applied stress level. Figure 18 presents SEM micrographs of the various regions of the fracture surface showing typical fatigue characteristics of striations in the crack-

propagation region (Fig. 23a) and dimples due to mircovoid coalescence in the final failure region, indicating ductile fracture mechanisms (Fig. 23b).

Figure 24 shows typical fracture surfaces observed for the BCC-HEAs. Striations can be seen at or near the tensile surface propagating perpendicular to the applied stress although they are much less prevalent in these alloys. The final fracture surface has a much different appearance than the FCC-HEAs. This area is characterized by cleavage-type fracture (Fig. 24a) and intergranular fracture (Fig. 24b) seen along the grain boundaries and. This is indicative of brittle failure mechanisms in these alloys.
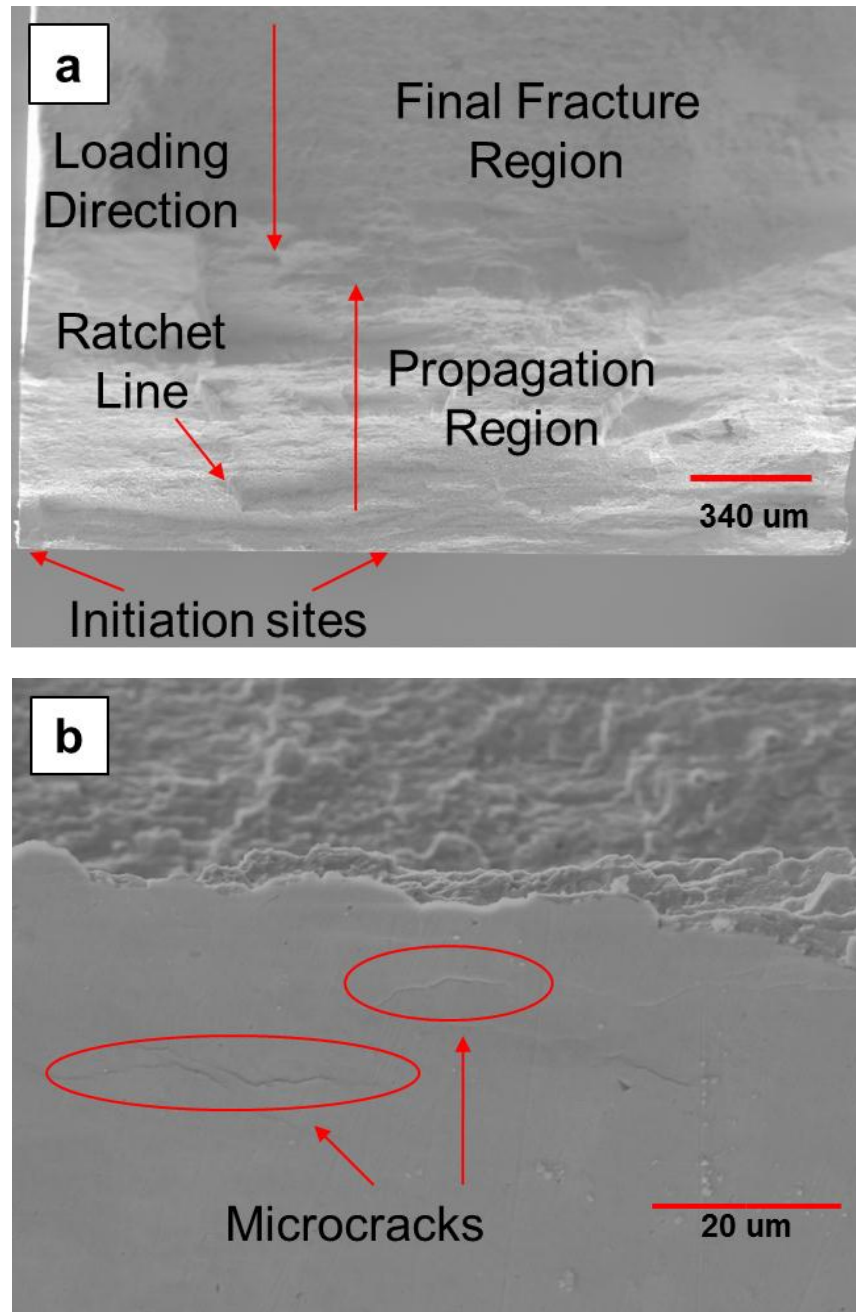
Figure 21. (a) SEM macrograph of the fracture surface of a sample that failed at a stress range of 900 MPa after 555,235 cycles. Crack initiation occurred at (b) the surface of the sample with microcracks formed before the fatigue test (Note that the loading direction comes out of the page).
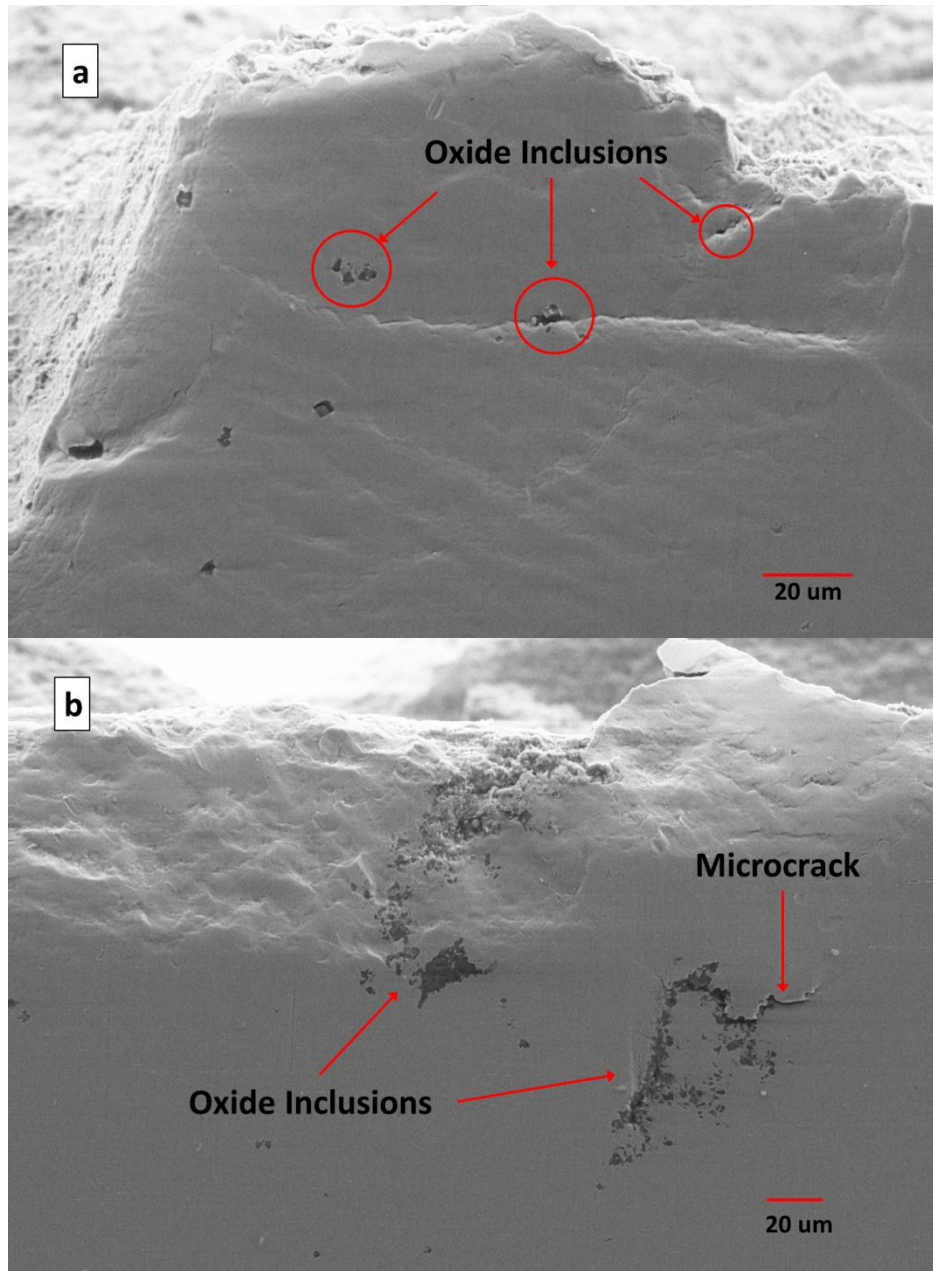
Figure 22. SEM micrograph of a typical tensile surface of the BCC-HEAs. a) Large oxide inclusions can be seen near fracture surface with a buildup of slip bands around them. b) Microcracks nucleating at large oxide particles.
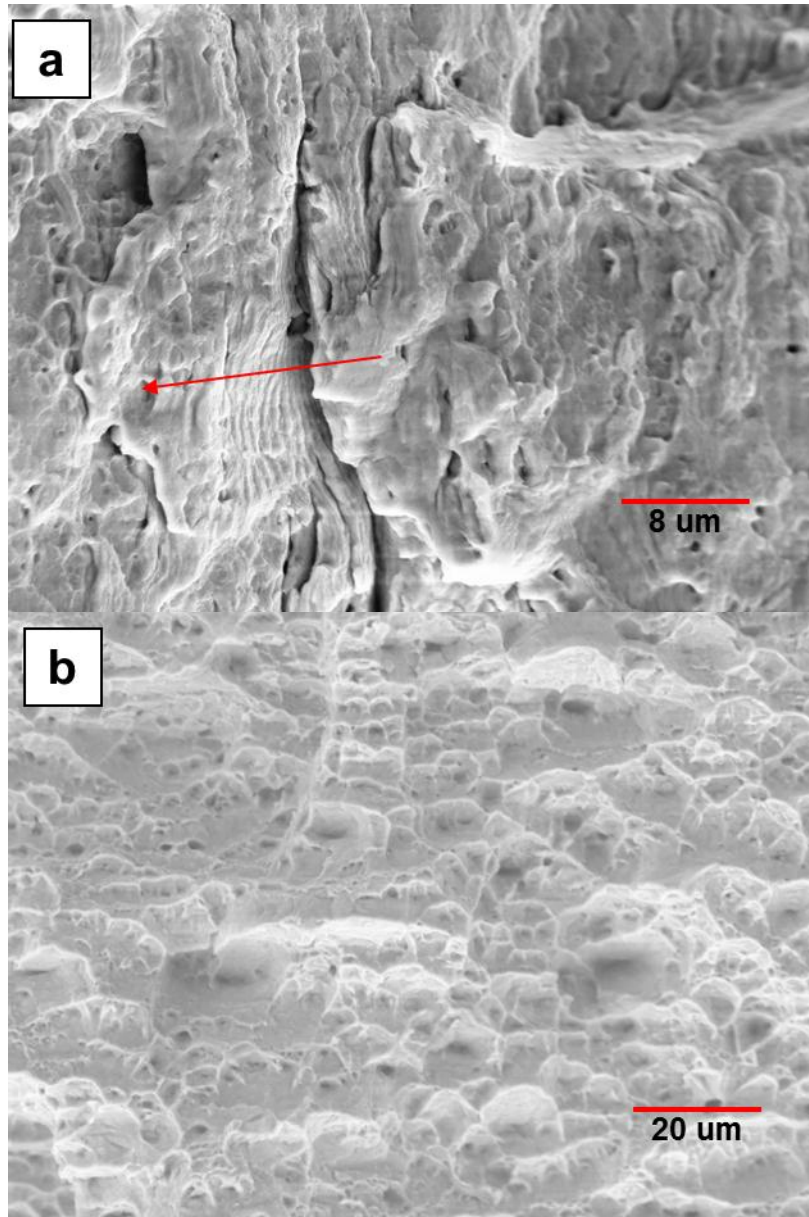
Figure 23. SEM micrographs of FCC-HEAs showing (a) fatigue striations in the crack-propagation region with the crack-growth direction indicated by the arrow and (b) dimples in the final fracture region, indicating a ductile fracture in the sample.
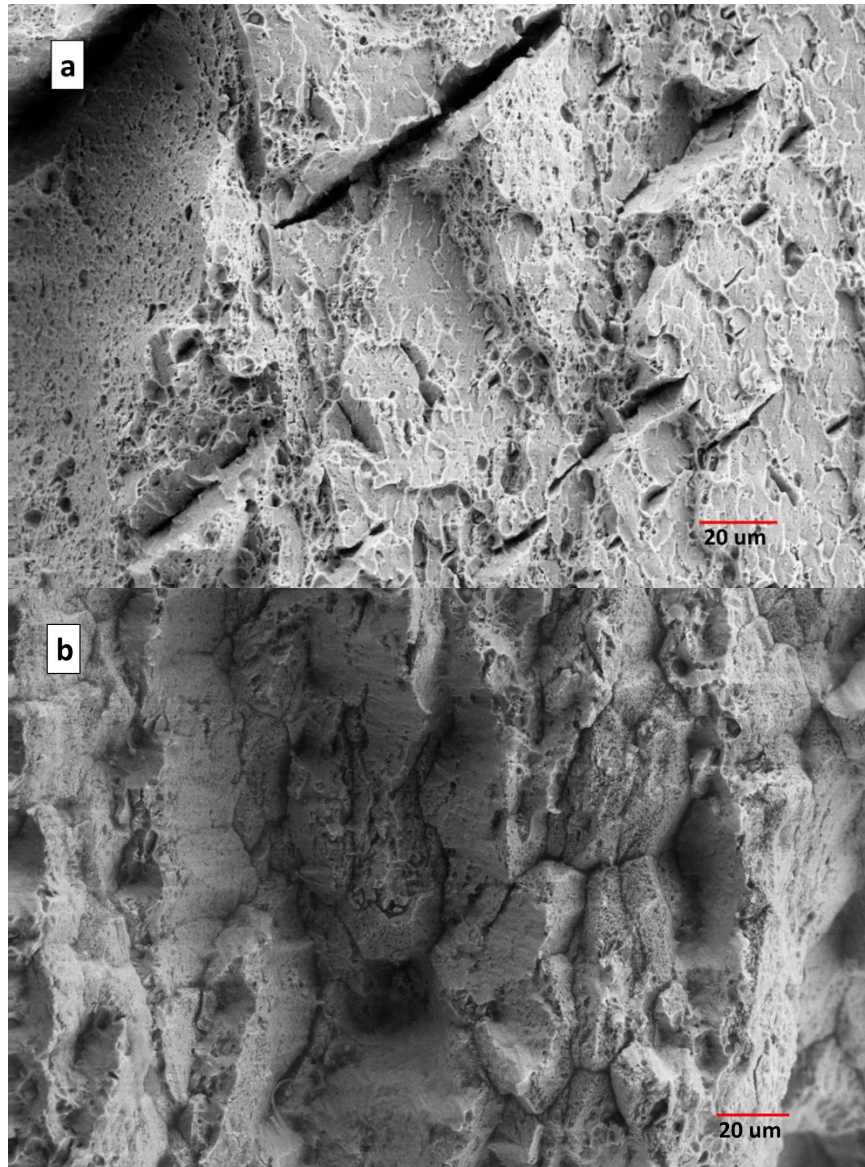
Figure 24. SEM micrographs of the fracture surface of BCC-HEAs showing a) cleavage fracture and b) intergranular fracture in the final failure region indicating a brittle fracture mechanism.

CHAPTER 3
PREDICTIVE MODELS FOR FATIGUE LIFE

3.1   Weibull Predictive Model

The phenomenon of fatigue is of stochastic nature [40]. Statistical models and data-analysis methods are, therefore, imperative tools for studying the fatigue behavior. In this investigation, statistical fatigue-life models were developed to predict the fatigue life of the HEAs. The Weibull model was only applied to $Al_{0.5}CoCrCuFeNi$ HEAs due to the number of samples required at each stress level. The first predictive model assumes a Weibull distribution to describe the fatigue-life distribution at each fixed stress range, and is based on a commonly used analytical representation of the S-N curve given by Equation 6 [41],

$$N(S) = cS^{-d}, \tag{6}$$

where S denotes the applied stress range, $N(S)$ is the expected fatigue-life cycles at the stress range level, S, and c and d are positive material parameters. Taking the natural logarithm on the S-N relation (Equation 6) results in

$$\log(N(S)) = \gamma_0 + \gamma_1 \log(S), \tag{7}$$

where $\gamma_0 = \log(c)$ and $\gamma_1 = -d$. The S-N relation given by Equations 6 and 7 provides a simple way to relate the effect of the stress applied on the test item to the number of cycles to fatigue failure [41]. It, however, does not capture the variability in the observed fatigue-life data. Equation 8 accounts for such variability, an error term, ε, is introduced to Equation 7, i.e.,

$$\log(N(S)) = \gamma_0 + \gamma_1 \log(S) + \varepsilon. \tag{8}$$

It can be assumed that the error term, ε, follows the standardized smallest extreme value distribution. The fatigue-life model then given by Equation 8 becomes a Weibull regression model [42]. The Weibull regression model can be written as an equivalent Weibull- accelerated life-testing model that is widely used in reliability engineering and lifetime data analyses [42]. The fatigue life at a given stress level, S, follows the Weibull distribution. The probability density function (pdf) and the cumulative distribution function of the Weibull distribution are described in Equations 9 and 10, respectively,

$$f(N(S) \mid \alpha(S), \beta) = \frac{\beta}{\alpha(S)} \left(\frac{N(S)}{\alpha(S)} \right)^{\beta-1} \exp\left(-\left(\frac{N(S)}{\alpha(S)} \right)^{\beta} \right) \tag{9}$$

$$F(N(S) \mid \alpha(S), \beta) = 1 - \exp\left(-\left(\frac{N(S)}{\alpha(S)} \right)^{\beta} \right) \tag{10}$$

where β is the Weibull shape parameter, and the Weibull scale parameter, $\alpha(S)$, depends on the stress, S, according to,

$$\log(\alpha(S)) = \gamma_0 + \gamma_1 \log(S). \tag{11}$$

In this experiment, four samples had not failed when the bending fatigue test was terminated at 10^7 cycles, and they became censored observations. The probability of obtaining a censored observation at the stress level, S, is given by Equation 12,

$$P(N(S) \geq N_c) = 1 - F(N_c \mid \alpha(S), \beta) = \exp\left(-\left(\frac{N_c}{\alpha(S)} \right)^{\beta} \right), \tag{12}$$

where N_c equals 10^7 cycles, denoting the censoring time of the experiment.

The first fatigue-life model, which will be called the Weibull predictive model, consists of two components; the Weibull distribution describing the fatigue-life variability at a fixed stress range, and the relation describing the stress dependence of the fatigue life, given by Equation 11. Note that lifetime distributions other than the Weibull distribution may be used. For example, if the error term, ε, in Equation 8 is assumed to be a standardized normal random variable, then the fatigue life, $N(S)$, at a given stress level, S, follows the lognormal distribution. This study assumes the Weibull distribution, because it is the most widely used lifetime distribution in reliability engineering and lifetime data analyses, and has been applied to model the fatigue behavior of a variety of materials, such as steels [43, 44], aluminum alloys [45], and metallic glasses [46, 47].

The Weibull predictive model has three unknown model parameters, β, γ_0, and γ_1, which can be estimated by the maximum likelihood method [42]. We denote the observed fatigue-life data by $\{(N_i, S_i, \delta_i), i = 1, 2,\ldots, m\}$, where m is the total number of samples tested, and N_i and S_i are, respectively, the fatigue-life cycles and the applied stress of the ith sample. The binary indicator variable, δ_i, equals 1 if N_i is a failure observation, and $\delta_i = 0$ if N_i is a censored observation. Given the observed fatigue-life data, the maximum likelihood method estimates the model parameters by maximizing the likelihood function given in Equation 13,

$$L(\beta,\gamma_0,\gamma_1) = \prod_{i=1}^{m} \left[\frac{\beta}{e^{\gamma_0+\gamma_1\log(S_i)}} \left(\frac{N_i}{e^{\gamma_0+\gamma_1\log(S_i)}} \right)^{\beta-1} \right]^{\delta_i} \exp\left[-\left(\frac{N_i}{e^{\gamma_0+\gamma_1\log(S_i)}} \right)^{\beta} \right]. \tag{13}$$

Once the model parameters are estimated, the fatigue-life behavior at a given stress, *S*, can be predicted by estimating the *p* quantile life, which is given by Equation 14,

$$N_p(S) = \exp(\gamma_0 + \gamma_1 \log(S))(-\log(1-p))^{1/\beta}.$$ (14)

The median fatigue life (i.e., *p* = 0.5) can be used to describe the relationship between the applied stress and the average fatigue-life response. The 2.5 and 97.5 quantiles can be employed to construct a 95% predictive interval for the fatigue life, and to quantify the scatter in the fatigue life cycles.

3.2 Weibull Mixture Predictive Model

The Weibull predictive model, however, may not be able to adequately characterize the excessive variability in the observed fatigue data shown in Figure 15. Especially, when the applied stress range is less than 1,000 MPa, the observed fatigue lives seem to form two groups, a strong group and a weak group. The fatigue lives in the weak group are much shorter than those in the strong group. This excessive variability in the fatigue data may be caused by the variability in the defect density in the experimental units, as discussed later. A Weibull mixture model (or called the multimodal Weibull model) may be used when the population of units is nonhomogeneous [48]. The second predictive model, therefore, assumes a mixture of two Weibull distributions for the fatigue lives at each stress range level. The pdf and cdf of the Weibull mixture model are given in Equations 15 and 16, respectively,

$$
\begin{aligned}
f(N(S) \mid p, \alpha_w(S), \beta_w, \alpha_s(S), \beta_s) = & \, p \frac{\beta_w}{\alpha_w(S)} \left(\frac{N(S)}{\alpha_w(S)} \right)^{\beta_w - 1} \exp\left(-\left(\frac{N(S)}{\alpha_w(S)} \right)^{\beta_w} \right) \\
& + (1-p) \frac{\beta_s}{\alpha_s(S)} \left(\frac{N(S)}{\alpha_s(S)} \right)^{\beta_s - 1} \exp\left(-\left(\frac{N(S)}{\alpha_s(S)} \right)^{\beta_s} \right),
\end{aligned}
\tag{15}
$$

$$
F(N(S) \mid p, \alpha_w(S), \beta_w, \alpha_s(S), \beta_s) = p \left[1 - \exp\left(-\left(\frac{N(S)}{\alpha_w(S)} \right)^{\beta_w} \right) \right] + (1-p) \left[1 - \exp\left(-\left(\frac{N(S)}{\alpha_s(S)} \right)^{\beta_s} \right) \right],
\tag{16}
$$

where the subscripts, w and s, denote the weak and strong groups, respectively, and the parameter, p, is the fraction of samples belonging to the weak group. The probability of obtaining a censored observation in the Weibull mixture model is then given by Equation 17,

$$P(N(S) > N_c) = p \exp\left[-\left(\frac{t}{\alpha_w(S)}\right)^{\beta_w}\right] + (1-p)\exp\left[-\left(\frac{t}{\alpha_s(S)}\right)^{\beta_s}\right]. \qquad (17)$$

Again, the Weibull scale parameters, $\alpha_w(S)$ and $\alpha_s(S)$, are assumed to be dependent on the stress, S, according to Equations 18 and 19,

$$\log(\alpha_w(S)) = \gamma_{w,0} + \gamma_{w,1} \log(S), \qquad (18)$$

and

$$\log(\alpha_s(S)) = \gamma_{s,0} + \gamma_{s,1} \log(S), \qquad (19)$$

respectively. The second fatigue-life model, called the Weibull mixture predictive model, has seven unknown parameters p, $\gamma_{w,0}$, $\gamma_{w,1}$, β_w, $\gamma_{s,0}$, $\gamma_{s,1}$, and β_s. The unknown parameters can again be estimated, using the maximum likelihood method. The likelihood function of the model parameters is given by Equation 20,

$$L(p, \beta_w, \gamma_{w,0}, \gamma_{w,1}, \beta_s, \gamma_{s,0}, \gamma_{s,1}) = \prod_{i=1}^{m} f(N_i)^{\delta_i} (1 - F(N_i))^{1-\delta_i}, \qquad (20)$$

where $f(N_i)$ and $F(N_i)$ are given by Equations 15 and 16, respectively. Once the maximum likelihood estimates of the seven model parameters are obtained, the observed fatigue data can be clustered into the two groups. If N_i is a failure observation, the likelihoods of the ith sample belonging to the weak group and the strong group are given by the expressions

$$\frac{\beta_w}{e^{\gamma_{w,0} + \gamma_{w,1} \log(S_i)}} \left(\frac{N_i}{e^{\gamma_{w,0} + \gamma_{w,1} \log(S_i)}}\right)^{\beta_w - 1} \exp\left(-\left(\frac{N_i}{e^{\gamma_{w,0} + \gamma_{w,1} \log(S_i)}}\right)^{\beta_w}\right)$$

and

$$\frac{\beta_s}{e^{\gamma_{s,0} + \gamma_{s,1} \log(S_i)}} \left(\frac{N_i}{e^{\gamma_{s,0} + \gamma_{s,1} \log(S_i)}}\right)^{\beta_s - 1} \exp\left(-\left(\frac{N_i}{e^{\gamma_{s,0} + \gamma_{s,1} \log(S_i)}}\right)^{\beta_s}\right),$$

respectively. The *i*th sample is then assigned to the group with a higher likelihood value. Similarly, if N_j is a censored observation, the likelihoods of the *j*th sample belonging to the two groups are given by

$$\exp\left(-\left(\frac{N_i}{e^{\gamma_{w,0}+\gamma_{w,1}\log(S_i)}}\right)^{\beta_w}\right) \text{ and } \exp\left(-\left(\frac{N_j}{e^{\gamma_{s,0}+\gamma_{s,1}\log(S_j)}}\right)^{\beta_s}\right),$$

respectively. The *p* quantile fatigue lives of the strong group and the weak group are predicted by Equations 21 and 22,

$$N_{p,w}(S) = \exp(\gamma_{w,0} + \gamma_{w,1}\log(S))(-\log(1-p))^{1/\beta_w}, \tag{21}$$

$$N_{p,s}(S) = \exp(\gamma_{s,0} + \gamma_{s,1}\log(S))(-\log(1-p))^{1/\beta_s}, \tag{22}$$

respectively.

3.3   General Log-Linear Model

This study also developed a third predictive model to study the correlation between the fatigue life and the type of morphology. A binary variable, X_i, is introduced to indicate the morphology type of the ith experimental unit, i.e., $X_i = 0$ for the parallel morphology, and $X_i = 1$ for the vertical morphology. A general log-linear model is assumed to describe the effect of the stress and the morphology on the Weibull scale parameter given in Equation 23,

$$\ln \alpha_i = \gamma_0 + \gamma_1 \log(S_i) + \gamma_2 X_i.$$

(23)

To determine whether the morphology affects the fatigue life, a test of significance can be performed on the regression coefficient, γ_2. The two hypotheses in the test of significance are H_0: $\gamma_2 = 0$ versus H_1: $\gamma_2 \neq 0$. If H_0 is rejected, there is evidence that the type of morphology affects the fatigue life. If the test of significance fails to reject H_0, there is no evidence against the hypothesis that the morphology does not affect the fatigue life.

3.4   Computational Results

The Weibull predictive model is first applied to analyze the observed fatigue-life data. The maximum likelihood estimates of the three model parameters are β = 0.492, γ_0 = 70.869, and γ_1 = -8.327. Figure 25 shows the predicted median, 0.025 quantile, and 0.975 quantile fatigue lives. The 2.5 and 97.5 quantiles are used to construct the 95% predictive interval for the fatigue life. This 95% predictive interval captures all the failure observations. This predictive interval, however, is very wide due to the excessive variability in the data and the limited sample size.
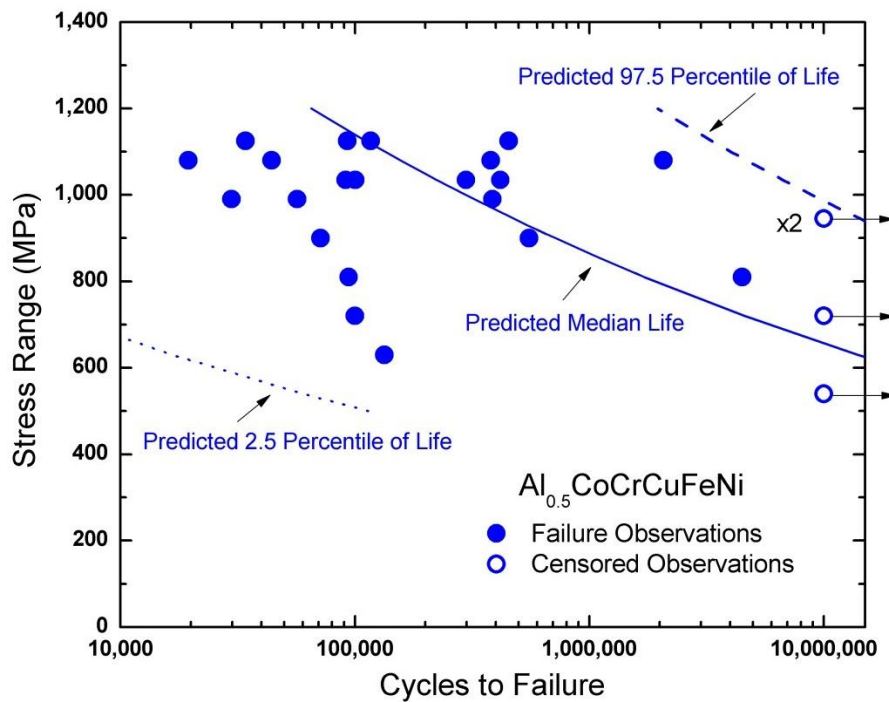
Figure 25. Predicted quantile lives by the Weibull predictive model.

Next, the Weibull mixture predictive model is used to analyze the experimental data. The maximum likelihood estimates of the seven model parameters are $p = 0.369$, $\beta_w = 3.773$, $\gamma_{w,0} = 15.238$, $\gamma_{w,1} = -0.555$, $\beta_s = 0.612$, $\gamma_{s,0} = 126.454$, and $\gamma_{s,1} = -16.245$. Figure 26 shows the predicted quantile lives by the Weibull mixture predictive model. The observed data are also clustered into the two groups. We are more interested in the strong group, because samples in the strong group contain less fabrication defects, and may, therefore, reveal the intrinsic fatigue behavior of the HEA, as discussed later. The median life of the strong group exceeds 10^7 cycles when the applied stress range is less than 858 MPa, which may be used as an estimate of the endurance limit of this HEA.
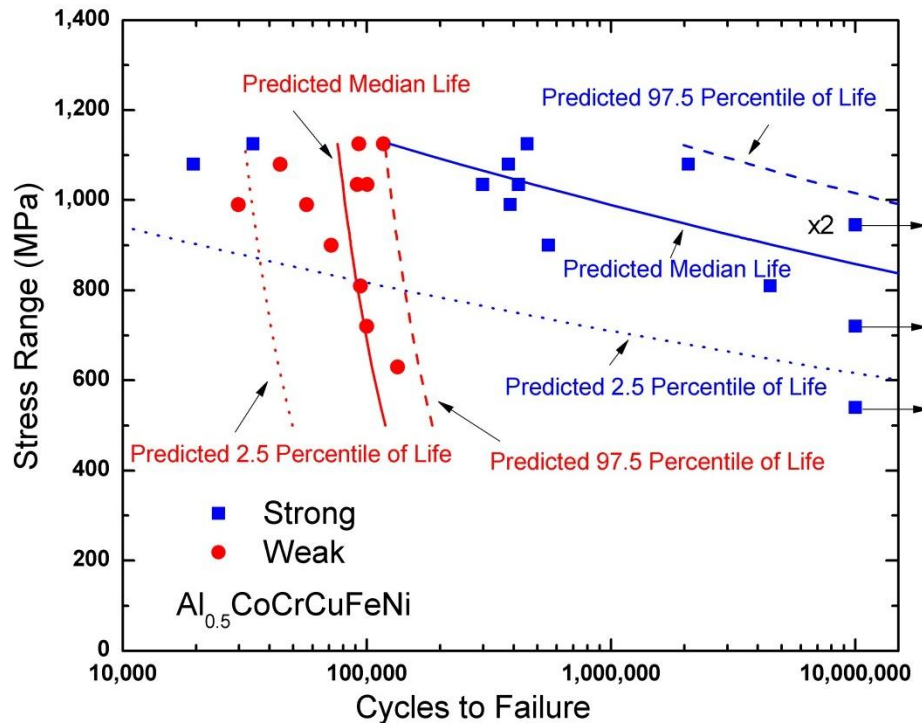
Figure 26. Predicted quantile lives by the Weibull mixture predictive model (Square symbol: observations in the weak group; Circular symbol: observations in the strong group).

49

When the applied stress ranges are 1,125 MPa, 1,080 MPa, and 1,035 MPa, there are four failure observations at each of the three stress levels. The Kolmogorov-Simirnov Goodness-of-Fit test is conducted to check if the Weibull distribution and the Weibull mixture distribution are appropriate for the fatigue-life data observed at these three stress levels. Table 2 summarizes the Kolmogorov-Simirnov test statistic values. Because all the test statistic values are less than the critical value of 0.494 [49], there is no evidence to reject the Weibull or the Weibull mixture model as an appropriate model for the data collected at these three stress levels. For the fatigue data collected at other stress levels, the Goodness-of-fit test is not conducted because of the very small sample sizes.

Table 2. Kolmogorov-Simirnov goodness-of-fit test for the Weibull and the Weibull mixture distributions.

Stress range (MPa)	Kolmogorov-Simirnov test statistics	
	Weibull distribution	Weibull mixture distribution
1,125	0.32	0.31
1,080	0.22	0.33
1,035	0.39	0.39

To determine which predictive model is better for the observed data, we apply three commonly-used model-selection criteria, i.e., the log-likelihood, the Akaike information criterion (AIC), and the Bayesian information criterion (BIC). The AIC and BIC are defined by Equations 24 and 25, respectively,

$$\mathrm{AIC} = 2\log L - 2k, \tag{24}$$

$$\mathrm{BIC} = 2\log L - k\log m, \tag{25}$$

where $\log L$, n, and k are the log-likelihood, the number of observations, and the number of parameters of a model, respectively. The log-likelihood measures how well a model fits the data. Using more complex models usually fits the data better. The AIC and the BIC, however, penalize the complexity of the model where the complexity refers to the number of parameters in a model. A model with a higher $\log L$, AIC, or BIC value is usually more preferred. Table 3 lists the three model-selection criteria for the two predictive models. All the three criteria indicate that the Weibull mixture predictive model is more preferred than the Weibull predictive model.

Table 3. Model selection between the Weibull predictive model and the Weibull mixture predictive model.

Model	Model-selection criteria		
	Log-likelihood, log$L$	AIC = 2log$L$-2k	BIC = 2log$L$-$k$log$m$
Weibull	-303.9	-613.7	-617.4
Weibull mixture	-293	-601.9	-610.5

It was thought that the microstructure, specifically the orientation of the α and β phases due to casting, could play an important role in affecting the fatigue characteristics. To study the relationship between the fatigue life and the morphology, the third predictive model is applied to analyze the observed fatigue-life data in the strong group. The Weibull distribution is used to model the variability in the fatigue life at a fixed stress level for the strong group, and the Weibull scale parameter is modeled by the general log-linear relation (Equation 23). The test of significance for the regression coefficient, γ_2, yields a *P*-value of 0.18. The test, hence, fails to reject H_0: $\gamma_2 = 0$ at the commonly used significance level of 0.05 or 0.10. Analysis of the observations in the weak group results in the same conclusion with a *P*-value of 0.73. Therefore, there is no evidence to indicate that the morphology affects the fatigue life.

CHAPTER 4
Discussion

4.1 Effect of Defects

Both the experimental results (Figs. 20 and 22) and the computational result (Figure 26) confirmed that the fatigue-life cycles of the HEA are mainly controlled by the defects. Figure 27 illustrates that the strong group tends to have less defects, on average, than the weak group. At a given stress level, the strong samples with less defects tend to exhibit longer fatigue lives than the weak samples with more defects. Therefore, the control of the defects during the fabrication processes is critically important for the future advancement and applications of the HEA. It is believed that a reduction in the number of these defects could result in more favorable fatigue behavior compared to that of conventional alloys.
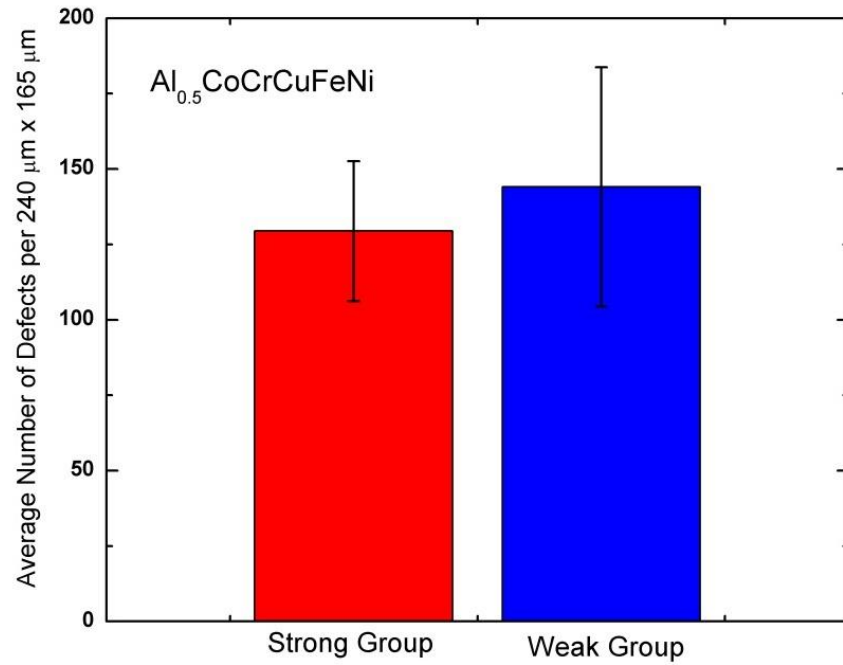
Figure 27. Bar-graph of the average number of defects observed for the weak and strong groups. The weak group tends to have more defects than the strong group, which can lead to shorter fatigue lifetimes.

4.2 Comparison of HEAs to Conventional Alloys

In total, four FCC-HEA specimens reached the endurance limit at stress ranges of 540 and 720 MPa, and two specimens at 945 MPa, respectively (Figure 15). These values correspond to excellent fatigue ratios (equal to the fatigue-endurance limit / UTS) between 0.402 and 0.703, respectively. The fatigue-endurance limit estimated by the Weibull mixture predictive model is 858 MPa for the strong group, which corresponds to a fatigue ratio of 0.638. These estimates show that FCC-HEAs have favorable and/or greater endurance limits and fatigue ratios comparable to steels, aluminum alloys, nickel alloys, titanium alloys, and bulk metallic glasses (BMGs), as shown in Table 4 and Figure 22 [27, 34, 36-38] and detailed below.

Two BCC-HEA specimens also did not fail throughout their fatigue lives at stress ranges of 540 and 630 MPa. The absence of tensile data prevents a normalized comparison of these alloys to other conventional alloys using the ultimate tensile strength. In general the BCC-HEAs tend to have a yield stress comparable to that of the FCC-HEAs at 1,254 and 1,284 MPa, respectively, described in Section 2.3. Shorter fatigue lives are comparable stress levels as well as lower estimates of the fatigue endurance limits seems to indicate that FCC-HEAs tend to outperform BCC-HEAs under fatigue conditions. That's not to say that BCC-HEAs perform poorly. In fact, a comparison of the endurance limits of BCC-HEAs to conventional alloys reveals that HEAs are comparable to most steels and outperform alloys with lower strengths.

55

Table 4. Comparison of the fatigue-endurance limits, ultimate strengths, and fatigue ratios (EL/UTS) of the $Al_{0.5}CoCrCuFeNi$ and $Al_{7.5}Cr_{22.5}Fe_{35}Mn_{20}Ni_{15}$ HEAs to various other alloys [34, 36-38].

| Material	Ultimate Tensile Strength (MPa)	Fatigue Endurance Limit (MPa)	Fatigue Ratio
HEA $Al_{0.5}CoCrCuFeNi$ (This study)	1,344	540/945	0.402/0.703
HEA $Al_{7.5}Cr_{22.5}Fe_{35}Mn_{20}Ni_{15}$ (This study)	N/A	540/630	N/A
4340 Steel (Quenched & Tempered 538°C) [37]	1,260	670	0.532
4340 Steel Annealed [37]	745	340	0.456
15-5PH Stainless Steel [37]	1,137	620	0.545
1015 Steel Annealed [37]	455	240	0.527
Ti-6Al-4V [37]	1,035	515	0.498
IN 625 Superalloy [37]	1,082	445	0.411
Al 6061 (T6) [37]	310	96	0.313
Zr Grade 702 [38]	430	155	0.36
Zr-based BMGs [34, 36]	1,480-1,900	239-983	0.161-0.517
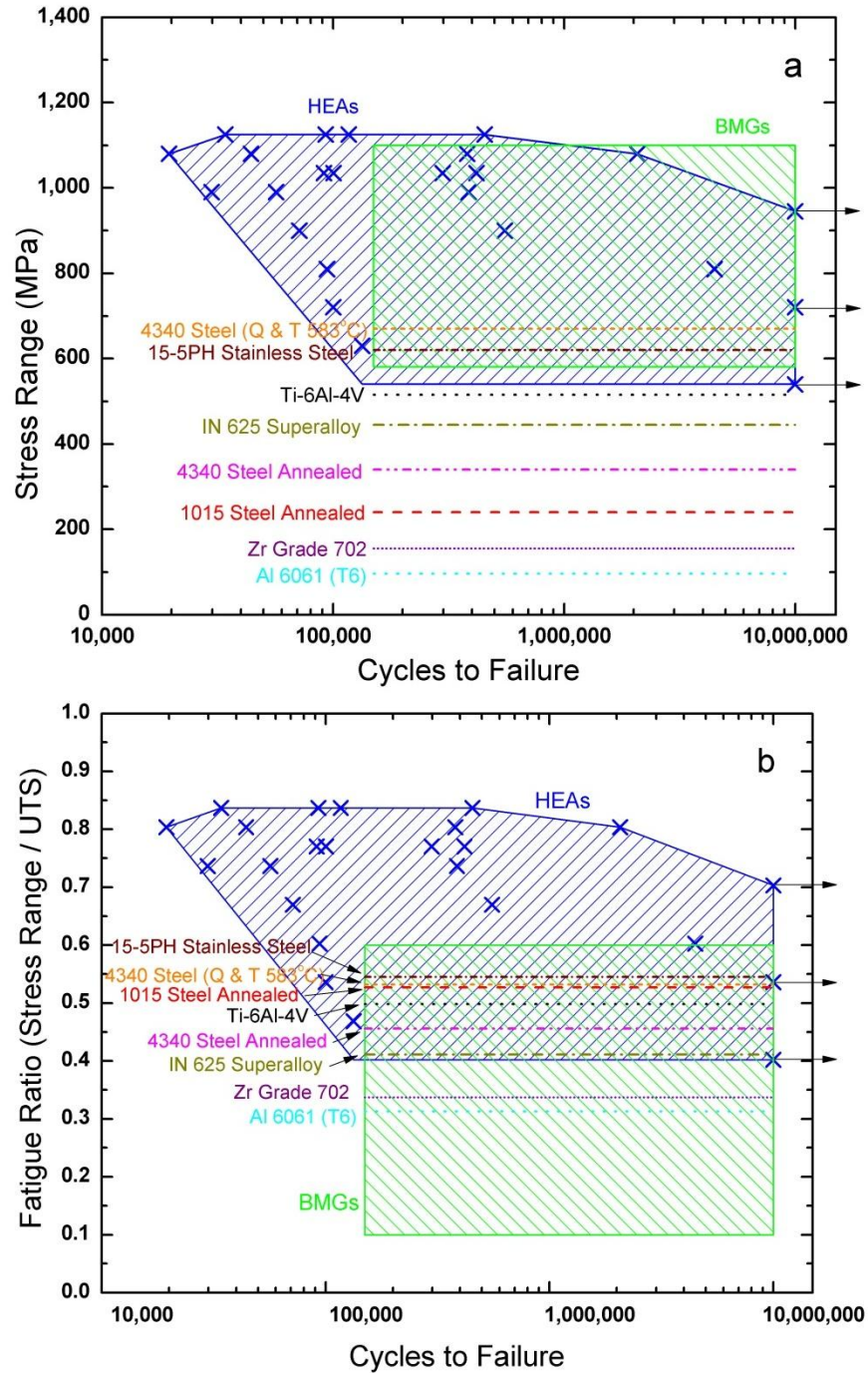
Figure 28. S-N curves comparing (a) the endurance limits and (b) the fatigue ratios of the $Al_{0.5}CoCrCuFeNi$ HEA, other conventional alloys, and bulk metallic glasses [27, 34, 36-38].

Figure 28a presents HEAs with the lower bound of the endurance limit comparable to 15-5PH stainless steel, 4340 steel, and titanium alloys, and the upper bound surpassed only by some BMGs. This trend is due to the extremely high UTS of BMGs (~ 1,900 MPa) relative to HEAs (1,344 MPa). Figure 23a illustrates this relationship when comparing the fatigue-endurance limit vs. UTS. One reason for the high fatigue strengths of FCC-HEAs is the high tensile strengths of these materials. It is clearly seen that as the UTS increases, the endurance limit will also increase in a linear fashion approximately equal to 0.5 for most materials [27]. FCC-HEAs follow a similar pattern and even exceed this ratio with an upper bound of 0.703 (Figs. 22b, 23b, and Table 4).

To better compare the fatigue performance of HEAs to materials relative to their UTS, the fatigue ratios are used and seen in Figure 23b, 24b, and Table 4. The lower bound of the fatigue ratios of HEAs compares favorably to those of steels, titanium, and nickel alloys, and outperforms the zirconium alloys as well as some of the Zr-based BMGs. Moreover, for some materials, such as ultra-high strength steels and wrought aluminum alloys, their high tensile strengths result in lower fatigue ratios due to their brittle nature [27]. The strong group of HEAs tends to outperform these materials by displaying a greater fatigue ratio than materials with comparable tensile strengths due to the reduced number of defects. The upper bound of the fatigue limit of HEAs is significantly higher than that of other conventional alloys and BMGs, showing that HEAs have the potential to outperform these materials in structural applications with improved fabrication and processing.
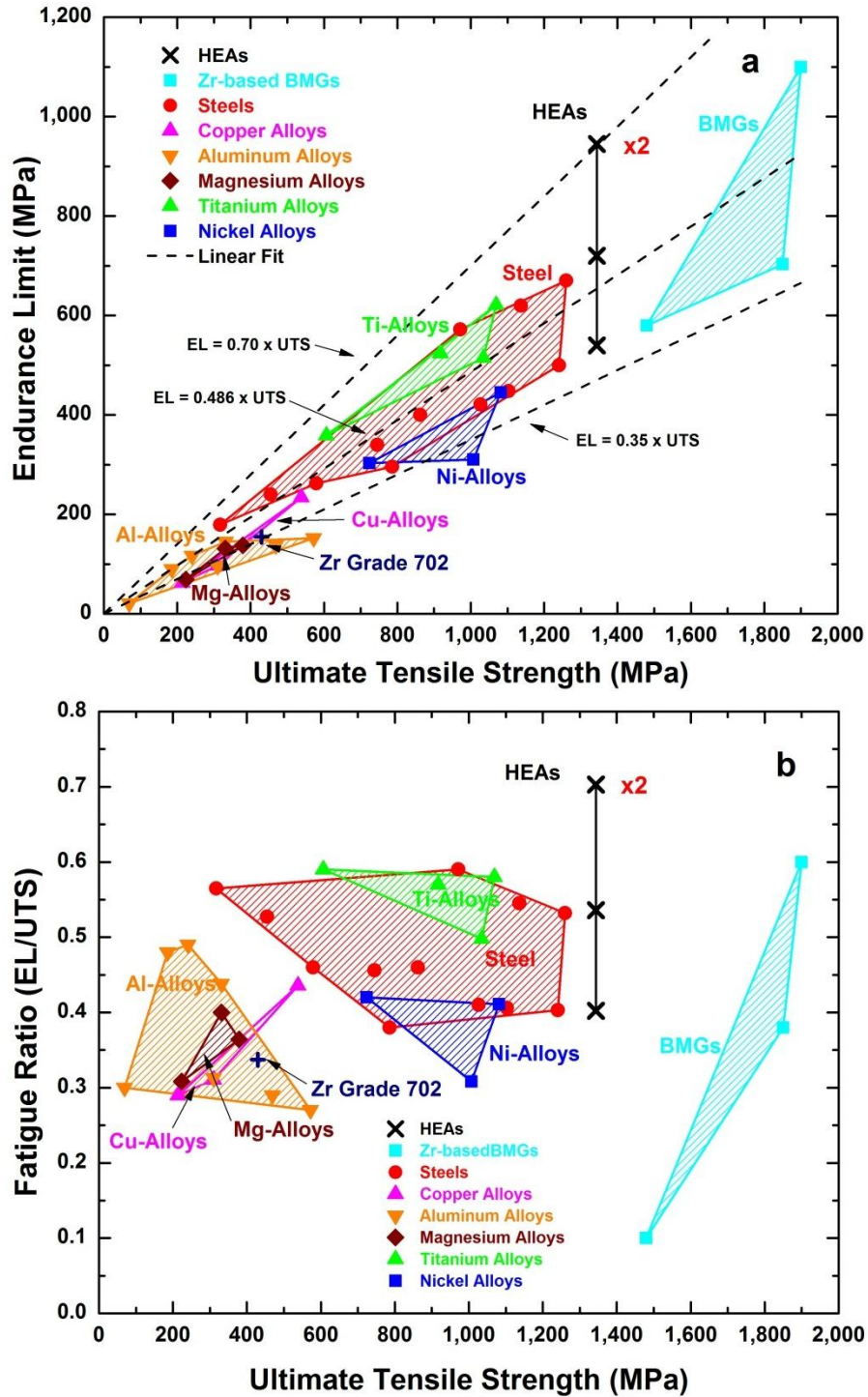
Figure 29. Plots comparing the (a) the endurance limits and (b) the fatigue ratios of the $Al_{0.5}CoCrCuFeNi$ HEA to as a function of the ultimate tensile strength of other structural materials and bulk metallic glasses [27, 34, 36-38].

CHAPTER 5
Conclusions

The fatigue studies show encouraging fatigue-resistance characteristics due to the long fatigue lives of various samples at relatively high stresses. The fatigue-endurance limit of FCC-HEAs was found to be between 540 and 945 MPa. The fatigue-endurance limit for BCC-HEAs was found to be between 540 and 630 MPa. Some scattering of the fatigue life was seen in the S-N curve. A possible explanation of the scatter can be attributed to the different defect densities of aluminum-oxide particles and microcracks introduced during the casting and rolling operations. A Weibull mixture predictive model was utilized and showed two main groups with the strong group having a predicted median time to failure of greater than 10^7 at 858 MPa.

The fatigue-endurance limit to ultimate-tensile strength ratio between 0.402 and 0.703 compares favorably to conventional materials, such as steels, nickel-, aluminum-, and titanium-alloys, and advanced BMGs. This trend may partially be due to the high tensile strength of FCC-HEAs, compared to these materials. However, when the fatigue ratios of these materials are compared, HEAs may surpass those of conventional alloys with a reduction in defects introduced during fabrication and processing. $Al_9Co_{18.2}Cr_{18.2}Cu_{18.2}Fe_{18.2}Ni_{18.2}$ and $Al_{7.5}Cr_{22.5}Fe_{35}Mn_{20}Ni_{15}$ HEAs show promising fatigue-resistance characteristics and may be useful in future applications where fatigue is a factor.

These results are very encouraging to future research, exhibiting the potential for excellent fatigue resistance in HEAs and with possible long fatigue

lives, even at stresses approaching the ultimate stress. Because of the lack of the literature on the fatigue behavior of HEAs, the focus of the continuing research should be placed on the data points that show an unexpectedly long fatigue life as well as other promising HEA compositions. If the necessary information on the fatigue resistance can be found as well as the development of a prediction model for fatigue specimens, HEAs have a promising future in numerous applications for components in fatigue environments.

LIST OF REFERENCES

[1] M.A. Hemphill, T. Yuan, G.Y. Wang, J.W. Yeh, C.W. Tsai, A. Chuang, P.K. Liaw, Acta Materialia, 60 (2012) 5723-5734.

[2] J.R. Davis, in, ASM International, Metals Park, OH, 1990.

[3] J.W. Yeh, S.K. Chen, S.J. Lin, J.Y. Gan, T.S. Chin, T.T. Shun, C.H. Tsau, S.Y. Chang, Advanced Engineering Materials, 6 (2004) 299-303.

[4] Y. Zhang, Y.J. Zhou, J.P. Lin, G.L. Chen, P.K. Liaw, Advanced Engineering Materials, 10 (2008) 534-538.

[5] Y.J. Zhou, Y. Zhang, Y.L. Wang, G.L. Chen, Materials Science and Engineering a-Structural Materials Properties Microstructure and Processing, 454 (2007) 260-265.

[6] J.W. Yeh, S.K. Chen, J.Y. Gan, S.J. Lin, T.S. Chin, T.T. Shun, C.H. Tsau, S.Y. Chang, Metallurgical and Materials Transactions a-Physical Metallurgy and Materials Science, 35A (2004) 2533-2536.

[7] C.J. Tong, Y.L. Chen, S.K. Chen, J.W. Yeh, T.T. Shun, C.H. Tsau, S.J. Lin, S.Y. Chang, Metallurgical and Materials Transactions a-Physical Metallurgy and Materials Science, 36A (2005) 881-893.

[8] P.K. Huang, J.W. Yeh, T.T. Shun, S.K. Chen, Advanced Engineering Materials, 6 (2004) 74-78.

[9] A. Takeuchi, N. Chen, T. Wada, Y. Yokoyama, H. Kato, A. Inoue, J.W. Yeh, Intermetallics, 19 (2011) 1546-1554.

62

[10] O.N. Senkov, G.B. Wilks, D.B. Miracle, C.P. Chuang, P.K. Liaw, Intermetallics, 18 (2010) 1758-1765.

[11] O.N. Senkov, G.B. Wilks, J.M. Scott, D.B. Miracle, Intermetallics, 19 (2011) 698-706.

[12] O.N. Senkov, J.M. Scott, S.V. Senkova, D.B. Miracle, C.F. Woodward, Journal of Alloys and Compounds, 509 (2011) 6043-6048.

[13] M.H. Chuang, M.H. Tsai, W.R. Wang, S.J. Lin, J.W. Yeh, Acta Materialia, 59 (2011) 6308-6317.

[14] C.Y. Hsu, W.R. Wang, W.Y. Tang, S.K. Chen, J.W. Yeh, Advanced Engineering Materials, 12 (2010) 44-49.

[15] L.H. Wen, H.C. Kou, J.S. Li, H. Chang, X.Y. Xue, L. Zhou, Intermetallics, 17 (2009) 266-269.

[16] T.T. Shun, C.H. Hung, C.F. Lee, Journal of Alloys and Compounds, 493 (2010) 105-109.

[17] C.J. Tong, M.R. Chen, S.K. Chen, J.W. Yeh, T.T. Shun, S.J. Lin, S.Y. Chang, Metallurgical and Materials Transactions a-Physical Metallurgy and Materials Science, 36A (2005) 1263-1271.

[18] F.J. Wang, Y. Zhang, G.L. Chen, H.A. Davies, International Journal of Modern Physics B, 23 (2009) 1254-1259.

[19] Y.F. Kao, T.J. Chen, S.K. Chen, J.W. Yeh, Journal of Alloys and Compounds, 488 (2009) 57-64.

[20] G.E. Dieter, Mechanical Metallurgy, McGraw-Hill, London, 1988.

[21] Y.P. Wang, B.S. Li, H.Z. Fu, Advanced Engineering Materials, 11 (2009) 641-644.

[22] C.W. Tsai, M.H. Tsai, J.W. Yeh, C.C. Yang, Journal of Alloys and Compounds, 490 (2010) 160-165.

[23] H.Y. Chen, C.W. Tsai, C.C. Tung, J.W. Yeh, T.T. Shun, C.C. Yang, S.K. Chen, Annales De Chimie-Science Des Materiaux, 31 (2006) 685-698.

[24] S.T. Chen, W.Y. Tang, Y.F. Kuo, S.Y. Chen, C.H. Tsau, T.T. Shun, J.W. Yeh, Materials Science and Engineering a-Structural Materials Properties Microstructure and Processing, 527 (2010) 5818-5825.

[25] C.W. Tsai, Y.L. Chen, M.H. Tsai, J.W. Yeh, T.T. Shun, S.K. Chen, Journal of Alloys and Compounds, 486 (2009) 427-435.

[26] R.W. Hertzberg, Deformation and Fracture Mechanics of Engineering Materials, 4th ed., John Wiley and Sons, Inc., New York, 1995.

[27] J.Y. Mann, Fatigue of Materials, Melbourne University Press, Victoria, 1967.

[28] ASM Handbook, Fatigue and Fracture, ASM International, 1996.

[29] W.D. Callister, Materials Science and Engineering: An Introduction, 7th ed., John Wiley and Sons, Inc., 2007.

[30] Z.Y. Liu, S. Guo, X.J. Liu, J.C. Ye, Y. Yang, X.L. Wang, L. Yang, K. An, C.T. Liu, Scripta Materialia, 64 (2011) 868-871.

[31] G.Y. Ke, S.K. Chen, T. Hsu, J.W. Yeh, Annales De Chimie-Science Des Materiaux, 31 (2006).

[32] Y. Zhang, S.G. Ma, J.W. Qiao, Metallurgical and Materials Transactions a-Physical Metallurgy and Materials Science, 43A (2012) 2625-2630.

[33] A.V. Kuznetsov, D.G. Shaysultanov, N.D. Stepanov, G.A. Salishchev, O.N. Senkov, Materials Science and Engineering a-Structural Materials Properties Microstructure and Processing, 533 (2012) 107-118.

[34] K.M. Flores, W.L. Johnson, R.H. Dauskardt, Scripta Materialia, 49 (2003) 1181-1187.

[35] C.P. Chuang, J.H. Huang, W. Dmowski, P.K. Liaw, R. Li, T. Zhang, Y. Ren, Applied Physics Letters, 95 (2009).

[36] G.Y. Wang, P.K. Liaw, Y. Yokoyama, A. Inoue, C.T. Liu, Materials Science and Engineering a-Structural Materials Properties Microstructure and Processing, 494 (2008) 314-323.

[37] Aerospace Structural Metals Handbook, CINDA/USAF CRDA Handbooks Operation, Purdue University, 2001.

[38] ASM Handbook, Properties and Selections: Nonferrous Alloys and Special Purpose Materials, ASM International, Metals Park, 1990.

[39] S. Singh, N. Wanderka, B.S. Murty, U. Glatzel, J. Banhart, Acta Materialia, 59 (2011) 182-190.

[40] B. Lehmayr, S. Staudacher, Fatigue & Fracture of Engineering Materials & Structures, 35 (2012) 347-358.

[41] F.G. Pascual, W.Q. Meeker, Technometrics, 41 (1999) 277-290.

[42] W.Q. Meeker, E. L.A., Statistical Methods for Reliability Data, Wiley, New York, 1998.

[43] H.D. Solomon, C. Amzallag, in: T.R. Allen, P.J. King, L. Nelson (Eds.) Proceedings from the 12th International Conference on Environmental

Degradation of Materials in Nuclear Power Systems – Water Reactors, TMS, Warrendale, PA, 2005, pp. 1091-1099.

[44] T. Sakai, T. Sakai, K. Okada, M. Furuichi, I. Nishikawa, A. Sugeta, International Journal of Fatigue, 28 (2006) 1486-1492.

[45] Q.G. Wang, D. Apelian, D.A. Lados, Journal of Light Metals, 1 (2001).

[46] Y.S. Zhang, T.; Mori, K., Journal of Solid Mechanics and Materials Engineering, 5 (2011).

[47] D.G. Harlow, P.K. Liaw, W.H. Peter, G.Y. Wang, R.A. Buchanan, Acta Materialia, 56 (2008) 3306-3311.

[48] D.G. Harlow, Acta Materialia, 59 (2011) 5048-5053.

[49] N. Mann, R. Schafer, N. Singpurwalla, Methods for Statistical Analysis of Reliability and Life Data, Wiley, New York, 1974.

Vita

Michael Hemphill was born on August 27, 1987 in Johnson City, TN to Bill and Jean Hemphill. He has one younger brother, Benjamin. He grew up in Johnson City attending St. Mary's School and Science Hill High School. He was cursed into growing up a Tennessee Volunteers fan due to his close family. He attended The University of Tennessee, Knoxville, made some great friends, and received a Bachelor of Science Degree in Materials Science and Engineering in December 2009. He continued his graduate studies at Tennessee and received his Master's Degree in Materials Science and Engineering in December 2012.